

Diet outperforms microbial transplant to drive microbiome recovery in mice

<https://doi.org/10.1038/s41586-025-08937-9>

Received: 1 August 2024

Accepted: 25 March 2025

Published online: 30 April 2025

 Check for updates

M. S. Kennedy^{1,2}, A. Freiburger^{3,10}, M. Cooper⁴, K. Beilsmith³, M. L. St George^{4,11}, M. Kalski^{4,12}, C. Cham⁴, A. Guzzetta⁵, S. C. Ng^{6,7}, F. K. Chan⁶, O. DeLeon⁴, D. Rubin⁸, C. S. Henry³, J. Bergelson^{9,13} & E. B. Chang^{4,13}✉

A high-fat, low-fibre Western-style diet (WD) induces microbiome dysbiosis characterized by reduced taxonomic diversity and metabolic breadth^{1,2}, which in turn increases risk for a wide array of metabolic^{3–5}, immune⁶ and systemic pathologies. Recent work has established that WD can impair microbiome resilience to acute perturbations such as antibiotic treatment^{7,8}, although little is known about the mechanism of impairment and the specific consequences for the host of prolonged post-antibiotic dysbiosis. Here we characterize the trajectory by which the gut microbiome recovers its taxonomic and functional profile after antibiotic treatment in mice on regular chow (RC) or WD, and find that only mice on RC undergo a rapid successional process of recovery. Metabolic modelling indicates that a RC diet promotes the development of syntrophic cross-feeding interactions, whereas in mice on WD, a dominant taxon monopolizes readily available resources without releasing syntrophic byproducts. Intervention experiments reveal that an appropriate dietary resource environment is both necessary and sufficient for rapid and robust microbiome recovery, whereas microbial transplant is neither. Furthermore, prolonged post-antibiotic dysbiosis in mice on WD renders them susceptible to infection by the intestinal pathogen *Salmonella enterica* serovar Typhimurium. Our data challenge widespread enthusiasm for faecal microbiota transplant (FMT) as a strategy to address dysbiosis, and demonstrate that specific dietary interventions are, at a minimum, an essential prerequisite for effective FMT, and may afford a safer, more natural and less invasive alternative.

Diet-induced dysbiosis predisposes the microbiome to collapse after antibiotic perturbation^{7,8}, but the relative contributions of diet and microbial community structure to this phenomenon are unknown, as is the extent to which the resultant dynamics can be explained by metabolic interactions. Microbial dysbiosis may reduce the availability of microorganisms to repopulate^{7,9,10}, and a poor resource environment may alter the ecology of recovery and community diversification^{11,12}. Understanding these dynamics is essential for selecting the most appropriate strategy for restoration of the microbiome. Here we compare microbiome resilience to and recovery after antibiotic perturbation across host diets, disentangle the effects of diet and microbial re-seeding on microbiome recovery, and propose a unified model of diet-driven ecological succession in restoration of the gut microbiome.

Microbiome recovery across diets

To determine how diet affects the resilience of the gut microbiome to antibiotic treatment, 86 female specific-pathogen-free (SPF) C57BL/6

mice were acclimatized to either a standard, low-fat, high-fibre diet (RC) or WD for four weeks. We then treated mice on each diet with either a triple antibiotic cocktail (Abx) or 5% PBS control in the drinking water for 72 h and collected faecal samples for 4 weeks, or for 9 weeks for a long-term cohort (Fig. 1a and Methods). One additional cohort of 12 male mice underwent the same protocol up to two weeks post-Abx to confirm that recovery patterns were consistent across the sexes (Extended Data Fig. 1b,c). Given that they were consistent across the sexes, we present analyses that include only female mice unless otherwise specified.

We first quantified resilience of the gut microbiome to antibiotic treatment in terms of microbial biomass by counting colony-forming units (CFUs) cultured on rich media. We found that CFU counts decreased rapidly after Abx treatment, but much more severely for the mice on WD (Fig. 1b and Supplementary Table 1). Whereas CFU counts for mice on RC had recovered to baseline levels by day 4 post-Abx, CFU counts for mice on WD did not recover to baseline up to at least day 7. Microbial biomass of PBS controls remained stable

¹Medical Scientist Training Program, Pritzker School of Medicine, The University of Chicago, Chicago, IL, USA. ²Department of Ecology & Evolution, The University of Chicago, Chicago, IL, USA.

³Division of Data Science and Learning, Argonne National Laboratory, Lemont, IL, USA. ⁴Department of Medicine, The University of Chicago, Chicago, IL, USA. ⁵Department of Pathology, The University of Chicago, Chicago, IL, USA. ⁶Microbiota I-Center (MagIC), Department of Medicine and Therapeutics, LKS Institute of Health Science, Institute of Digestive Disease, Center for Gut Microbiota Research, The Chinese University of Hong Kong, Hong Kong SAR, China. ⁷New Cornerstone Science Laboratory, The Chinese University of Hong Kong, Hong Kong, China. ⁸Inflammatory Bowel Disease Center, University of Chicago Medicine, Chicago, IL, USA. ⁹Department of Biology, Center for Genomics and Systems Biology, New York University, New York, NY, USA. ¹⁰Present address: Department of Chemical Engineering, Northwestern University, Evanston, IL, USA. ¹¹Present address: Medical Scientist Training Program, University of Illinois Chicago, Chicago, IL, USA.

¹²Present address: Stritch School of Medicine, Loyola University Chicago, Chicago, IL, USA. ¹³These authors jointly supervised this work: J. Bergelson, E. B. Chang. ✉e-mail: echang@bsd.uchicago.edu

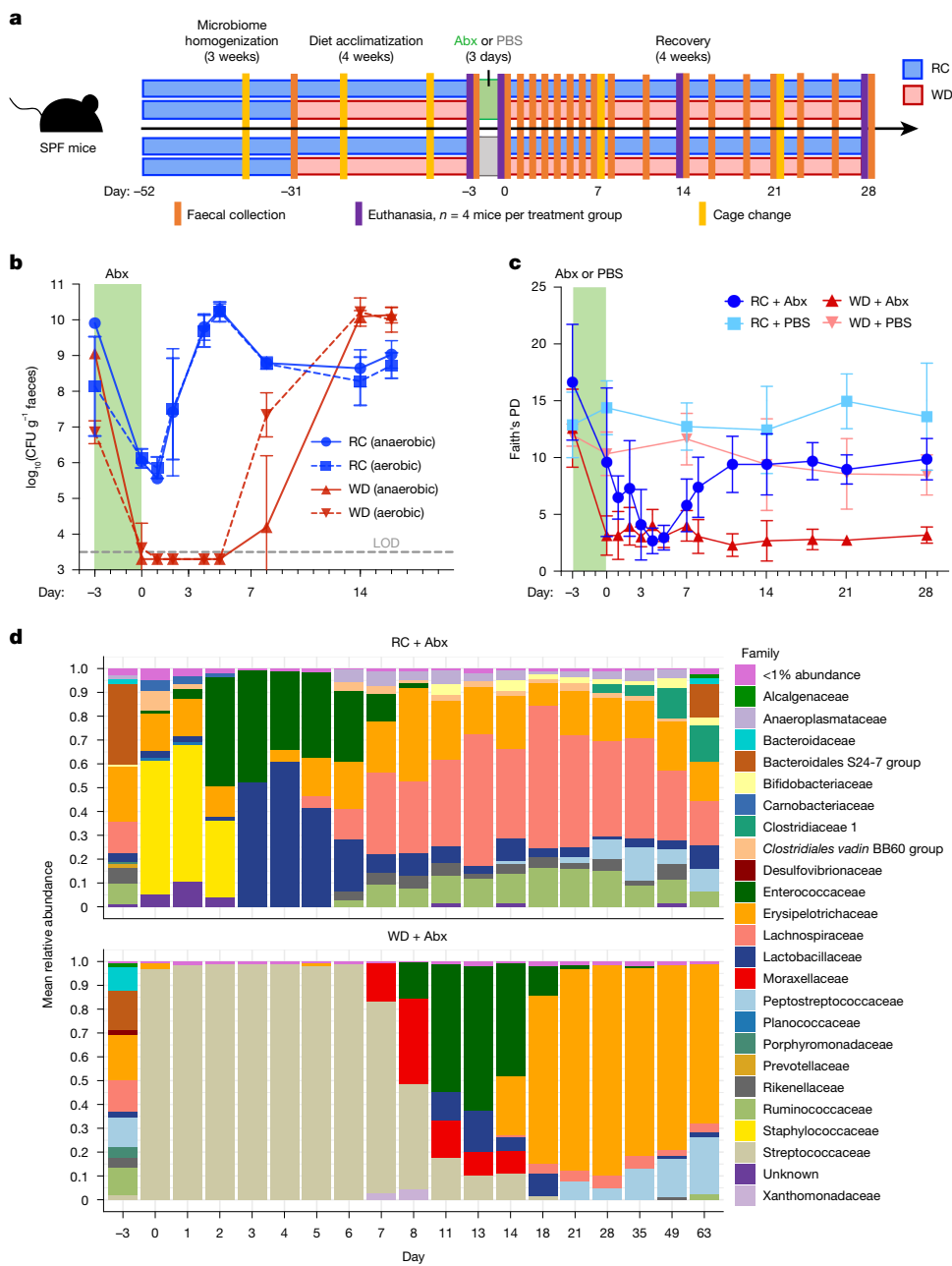


Fig. 1 | Bacterial biomass and taxonomic recovery after antibiotic treatment are impaired in mice on WD. **a**, Mice on RC or WD were treated with PBS or Abx in the drinking water for 72 h, and serial faecal samples were collected to assess microbiome recovery (Methods). **b**, Faecal microbial biomass in mice on RC-Abx and WD-Abx for mice from cohort 1 ($n = 6$ biologically independent mice per group). Data are mean \pm s.d. Statistics, including exact n and P values, are

presented in Supplementary Tables 1. See also Extended Data Fig. 1b,c. LOD, limit of detection. **c**, Faecal alpha diversity (Faith's phylogenetic diversity (PD)) of mice across dietary treatments and timepoints (all cohorts, $n = 4$ to 13 per group; exact n and P values are presented in Supplementary Table 2). Data are mean \pm s.d. **d**, Mean relative abundances of different microbial families for cohort 1 ($n = 6$ mice per group; see Extended Data Fig. 1i for other cohorts).

for both dietary treatments (Extended Data Fig. 1b and Supplementary Table 1).

We next evaluated taxonomic recovery of the gut microbiome across treatment groups using 16S ribosomal RNA (rRNA) gene sequencing. Immediately prior to antibiotic treatment (day -3), mice on WD exhibited significantly reduced phylogenetic diversity compared with mice on RC (Fig. 1c and Supplementary Table 2). Mice on both diets experienced a sharp decline in phylogenetic diversity after antibiotic treatment. RC-Abx mice began to recover phylogenetic diversity after day 5, and recovered more than half of their initial diversity by day 11. For WD-Abx mice, phylogenetic diversity remained severely diminished up to at least day 28 in all cohorts, and up to 9 weeks post-Abx. Phylogenetic

diversity in PBS controls did not change significantly. Other metrics of alpha diversity recapitulated these trends (Extended Data Fig. 1d-f and Supplementary Table 2).

Correspondingly, relative abundances of taxa were substantially altered during and after Abx treatment for mice on both diets (Fig. 1d). In RC-Abx mice, the microbiota passed through successive stages of recolonization, marked by early dominance of facultative anaerobes such as Enterococcaceae and Lactobacillaceae, followed by increasing diversification of stricter anaerobes. In WD-Abx mice, the low-biomass post-Abx community was dominated by Streptococcaceae until biomass started to recover. Recovery in WD-Abx mice also passed through a successional phase of facultative anaerobes, including Moraxellaceae,

Enterococcaceae and Lactobacillaceae, around day 14, before recovering stricter anaerobes. Although not all specific compositional changes were precisely replicated across cohorts (Extended Data Fig. 1*i*), certain characteristics, such as the early dominance of facultative anaerobes as biomass recovers and the post-Abx dominance of *Lactococcus* within the Streptococcaceae family in all WD-Abx groups, were consistent.

Principal coordinate analysis (PCOA) of Bray–Curtis dissimilarity revealed that microbiome dynamics track a similar compositional trajectory within treatment groups across all experimental cohorts (Extended Data Fig. 1*g–j*). By day 14 or earlier, the gut microbiota of mice on RC-Abx approached their respective pre-Abx community and corresponding RC-PBS controls, whereas the gut microbiota of WD-Abx mice remained distinct from their pre-Abx community at day 14. By day 28, while the microbiota of RC-Abx mice was indistinguishable from RC-PBS controls, only some mice on WD-Abx began to approach their initial community structure (PERMANOVA; Supplementary Table 2). These results indicate that mice on WD experience markedly impaired recovery of gut microbial taxonomic and biomass recovery after antibiotic treatment compared with mice on RC.

Microbiome functional capacity

To determine whether incomplete taxonomic recovery was associated with altered functional capacity, we performed shotgun metagenomic sequencing on faecal samples from a subset of mice on RC-Abx and WD-Abx at key timepoints before antibiotic treatment and throughout recovery (Methods). Gene calls were annotated with the Kyoto Encyclopedia of Genes and Genomes (KEGG) catalogue for functional interpretation.

We first evaluated gut microbiome functional diversity by calculating functional richness at different hierarchical levels (gene call, KEGG Ortholog (KO) or KEGG Category (KCat)) (Extended Data Fig. 2*a*). At the level of gene calls, mice on WD had reduced functional richness compared with mice on RC even before antibiotic treatment (Supplementary Table 3). After antibiotics, functional richness of mice on both diets collapsed severely, but whereas mice on RC recovered up to 69% of their initial gene count by day 28, mice on WD recovered only 16% of the initial gene count.

At broader hierarchical levels such as KO or KCat, functional richness was more preserved during and after antibiotic treatment across both treatment groups (Extended Data Fig. 2*a*). This could indicate a change in functional redundancy—that is, the number of unique gene calls that map to each KO—before and after antibiotic treatment. High functional redundancy would provide robustness at the KO level to the loss of individual gene calls. Indeed, we observe that mice on RC have greater functional redundancy before antibiotics and recover significantly more functional redundancy afterwards, whereas the loss of functional redundancy in mice on WD persists (Fig. 2*a* and Supplementary Table 3). In mice on RC, there was a much stronger correlation between initial and final functional redundancy across KOs than in mice on WD (Extended Data Fig. 2*b* and Supplementary Table 3), which tended to lose functional redundancy regardless of how much redundancy a given KO began with. To assess whether recovery of functional redundancy differed across functional subsystems, we mapped KOs with strong (more than 75%) or poor (less than 25%) recovery of functional redundancy at the KEGG system level (Fig. 2*b*). Although there were many more KOs that exhibited poor recovery in mice on WD and the majority (55%) of these mapped to metabolic functions, the proportional breakdown of KEGG systems was nearly identical across treatment groups and recovery levels (Fig. 2*b*). Thus, mice on WD experience a loss in functional diversity and redundancy after antibiotic treatment that varies in intensity across KO groups, with major losses in metabolic redundancy.

To focus on the most functionally interpretable aspects of our data, all subsequent metagenomic analyses were performed at the KO level.

We performed pairwise comparisons between the pre-Abx timepoint and all post-Abx timepoints to investigate functional characteristics of the microbiome throughout recovery, and to identify differentially abundant KOs. Mice on RC had 658 significantly depleted KOs at day 2 relative to pre-Abx, which grew to 835 depleted KOs at day 4, but nearly all of these recovered to baseline levels by day 14 (Extended Data Fig. 2*c* and Supplementary Table 4). At day 2 and day 4, semi-overlapping but distinct subsets of genes were enriched or depleted (Extended Data Fig. 2*d,e*), indicating unique intermediate functional stages during recovery.

Mice on WD had a larger number of significantly depleted KOs than RC counterparts at all timepoints evaluated, and even by day 28, 291 KOs had not yet returned to pre-Abx levels (Extended Data Fig. 2*f* and Supplementary Table 4). In contrast to mice on RC, the KOs depleted at day 14 and day 28 were almost all a subset of the KOs depleted at day 2 (Extended Data Fig. 2*g*). Mice on WD also had small, semi-overlapping sets of KOs that were significantly enriched relative to pre-Abx at all timepoints (Extended Data Fig. 2*h*). Further analysis of specific functional representation across timepoints and diets is presented in Extended Data Fig. 2*i–n* and Supplementary Table 4.

WD impairs metabolome recovery

To directly assay the resource environment of the gut, we performed a targeted faecal metabolomic screen of gut microbiome-associated compounds, including amino acids, carbohydrates, bile acids and others, from mice on RC-Abx and WD-Abx before and after antibiotic treatment. We found that for mice on RC, the normalized abundances of many compounds were distinct from baseline immediately after Abx, but that by day 11, the profile returned to baseline (Fig. 2*c*). This was statistically confirmed by PCOA clustering analysis (Extended Data Fig. 3*b,c* and Supplementary Table 5). Our heat map and PCOA revealed two inflection points during recovery: after day 3 and after day 7. The shift after day 3 is driven largely by the dynamics of raffinose and melibiose, two plant-derived α -galactoside compounds that are highly abundant in the RC diet¹³. The abundances of these compounds were markedly increased after antibiotics and up to day 3 but returned to baseline by day 5. The second shift reflects the dynamics of many compounds—including carbohydrate monomers such as ribose, glucose and arabinose, and many fatty acids—that are depleted after antibiotics but recover between day 7 and day 11. The secondary bile acids lithocholic acid, deoxycholic acid and 1,2-ketolithocholic acid, and to a lesser extent, the primary bile acid cholic acid were also depleted up to day 7, but were more abundant than baseline by day 11. In stark contrast, the metabolomic profile of mice on WD showed almost no signs of recovery up to day 14 (Fig. 2*c* and Extended Data Fig. 3*b,c*). Bile acids were heavily depleted throughout sampling. Sucrose, niacin and fatty acids, all of which were initially depleted in mice on RC but recovered after day 7, remained depleted throughout sampling for mice on WD. Carbohydrates such as cellobiose, arabinose and myo-inositol were overly abundant relative to baseline and did not return to baseline levels.

Because short-chain fatty acids (SCFAs) are well documented products of microbial metabolism and directly affect the host, we performed separate metabolomic analyses to quantify absolute levels of SCFAs in caecal samples from mice on RC-Abx and WD-Abx. The concentrations of acetate, butyrate and propionate at day 14 and day 28 in mice on RC were statistically indistinguishable from those pre-Abx, whereas for WD mice, they were depleted at day 14 and persisted at low levels up to day 28 (Fig. 2*d,f* and Supplementary Table 5).

We considered whether observed changes in metabolite abundances correspond to changes in abundances of microbial genes that produce or degrade those compounds. To assess this possibility, we plotted the relative abundances of several curated subsets of microbial genes across timepoints and overlaid the abundances of the associated metabolites (Methods). For example, melibiose and raffinose contain

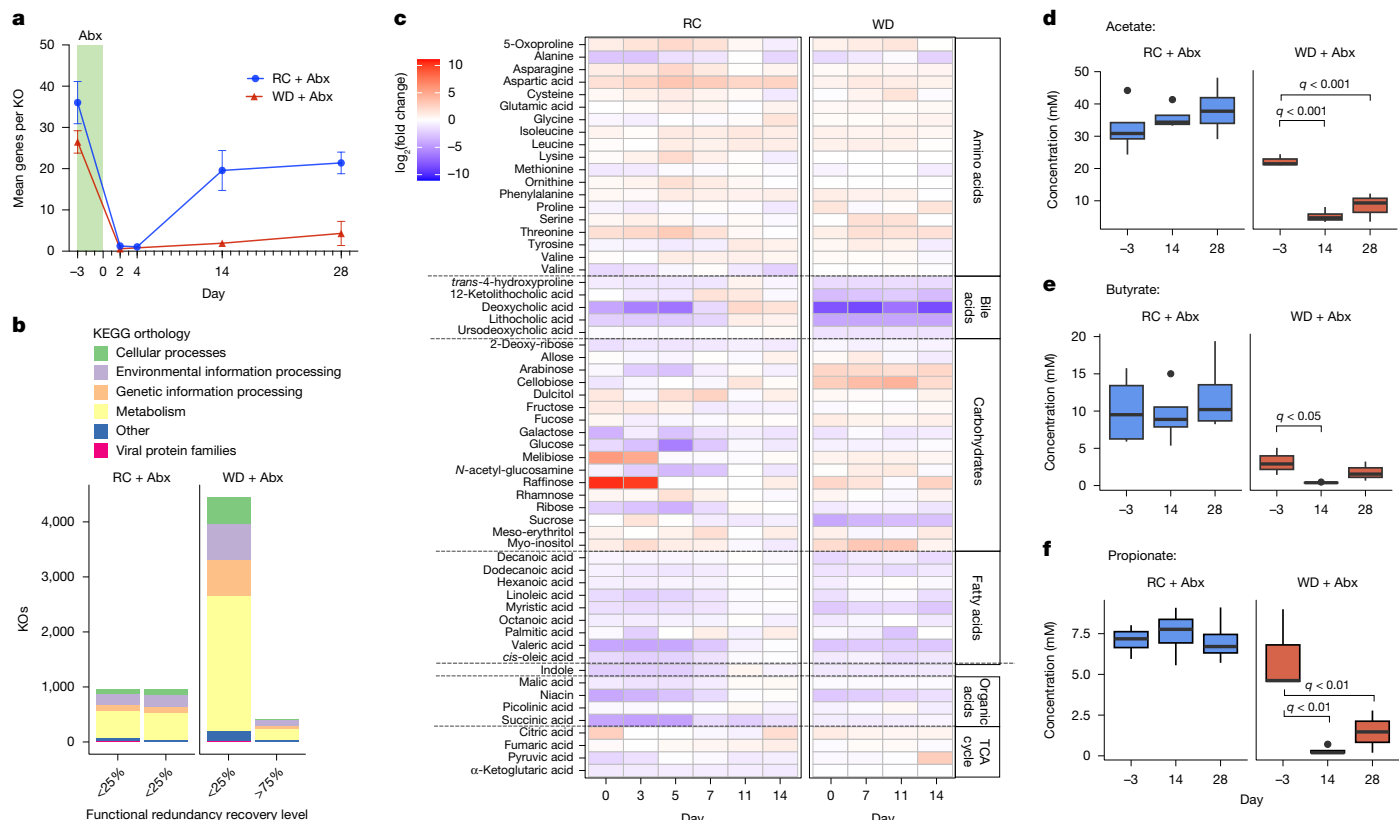


Fig. 2 | Functional recovery is severely impaired in mice on WD. **a**, Functional redundancy (mean genes per KO) of mice on RC-Abx and WD-Abx (RC-Abx day -3: $n = 8$; RC-Abx day 2: $n = 2$; RC-Abx day 4: $n = 3$; RC-Abx day 14: $n = 3$; RC-Abx day 28: $n = 3$; WD-Abx day -3: $n = 8$; WD-Abx day 2: $n = 3$; WD-Abx day 14: $n = 4$; WD-Abx day 28: $n = 3$). Data are mean \pm s.d. Statistics, including exact P values, are presented in Supplementary Table 3. **b**, KEGG system mapping of KOs that recovered less than 25% or more than 75% of their pre-Abx day -3 functional redundancy across RC-Abx and WD-Abx groups. **c**, Heat map displaying log₂-transformed fold change in metabolite abundances relative to the pre-Abx day -3 timepoint, averaged across $n = 3$ to 6 mice per group. Data for individual mice

are presented in Extended Data Fig. 3a. TCA, tricarboxylic acid. **d–f**, Absolute concentrations of acetate (**d**), butyrate (**e**) and propionate (**f**) in mice on RC-Abx (blue) and WD-Abx (red) (RC-Abx day -3, day 14 and day 28, and WD-Abx day 14: $n = 4$ mice per group; WD-Abx day -3, day 28: $n = 3$ mice per group; ANOVA with multiple post hoc comparisons and false discovery rate correction. Statistics, including exact q values, are presented in Supplementary Table 5. In box plots, the centre line is the median, the top and bottom hinges reflect the first and third quartiles, respectively, and the whiskers extend to 1.5 times the interquartile range. Data beyond the whiskers are plotted as individual points.

an α -1,6 linkage that can be hydrolysed by bacterial α -galactosidase genes but not by host enzymes¹³. In mice on RC, melibiose and raffinose reach higher concentrations after antibiotics when microbial α -galactosidase genes are most depleted, and as these genes recover, melibiose and raffinose abundances fall (Extended Data Fig. 3d and Supplementary Table 6). In mice on WD, we observe few changes in the abundance of α -galactosidase genes or the abundance of melibiose or raffinose. Starch and arabinan can similarly be metabolized into glucose and arabinose monomers, respectively. In mice on RC, both glucose and arabinose reach low abundance when genes for starch and arabinose metabolism drop, and as those polysaccharide metabolism genes increase in abundance, so does the abundance of the respective monomeric breakdown product (Extended Data Fig. 3e,f). In mice on WD, there are again few changes in either metabolite or gene abundances over the course of recovery. These data suggest that in mice on RC diet, the microbiota may respond to or interact with the resource environment, especially with complex carbohydrates, in a way that the microbiota of mice on WD does not.

Metabolic modelling of recovery dynamics

Across all taxonomic and functional metrics that we evaluated, mice on WD experienced more severe ecosystem collapse with slower and less complete recovery than mice on RC (Figs. 1 and 2). This was not

attributable to slower antibiotic clearance in mice on WD (Extended Data Fig. 4 and Supplementary Table 7). To explore the mechanism by which resource environment shapes community recovery patterns, we developed metabolic models that leverage functional knowledge of microbiome members and integrated omics data to predict the metabolic interactions and dynamics of each community over time (Methods). Most of the amplicon sequence variants (ASVs) presented in Fig. 1 closely match 16S sequences found in at least one fully annotated isolate genome in RefSeq, which we used to reconstruct representative probabilistic genome-scale metabolic models (prGEMs) through the ModelSEED2 pipeline¹⁴ in KBase (Supplementary Methods). Characterization of the metabolic potential of individual prGEMs (strain–metabolite interaction probability profiles; Extended Data Fig. 5) and abundance-weighted sample-wide communities (microbiome–metabolite interaction probability profiles) is available in the Supplementary Discussion.

To predict which metabolic functions were performed by which ASVs over the course of recovery and how this differed across diets, we next combined our ASV-based prGEMs into community models, and for each interval between timepoints, simulated the flux through each metabolic pathway within the constraints of our observed metabolite and ASV abundance dynamics. These simulations determined the most likely metabolic behaviour of the ASVs in each interval (Extended Data Fig. 6 and Supplementary Table 8), and revealed profound metabolic

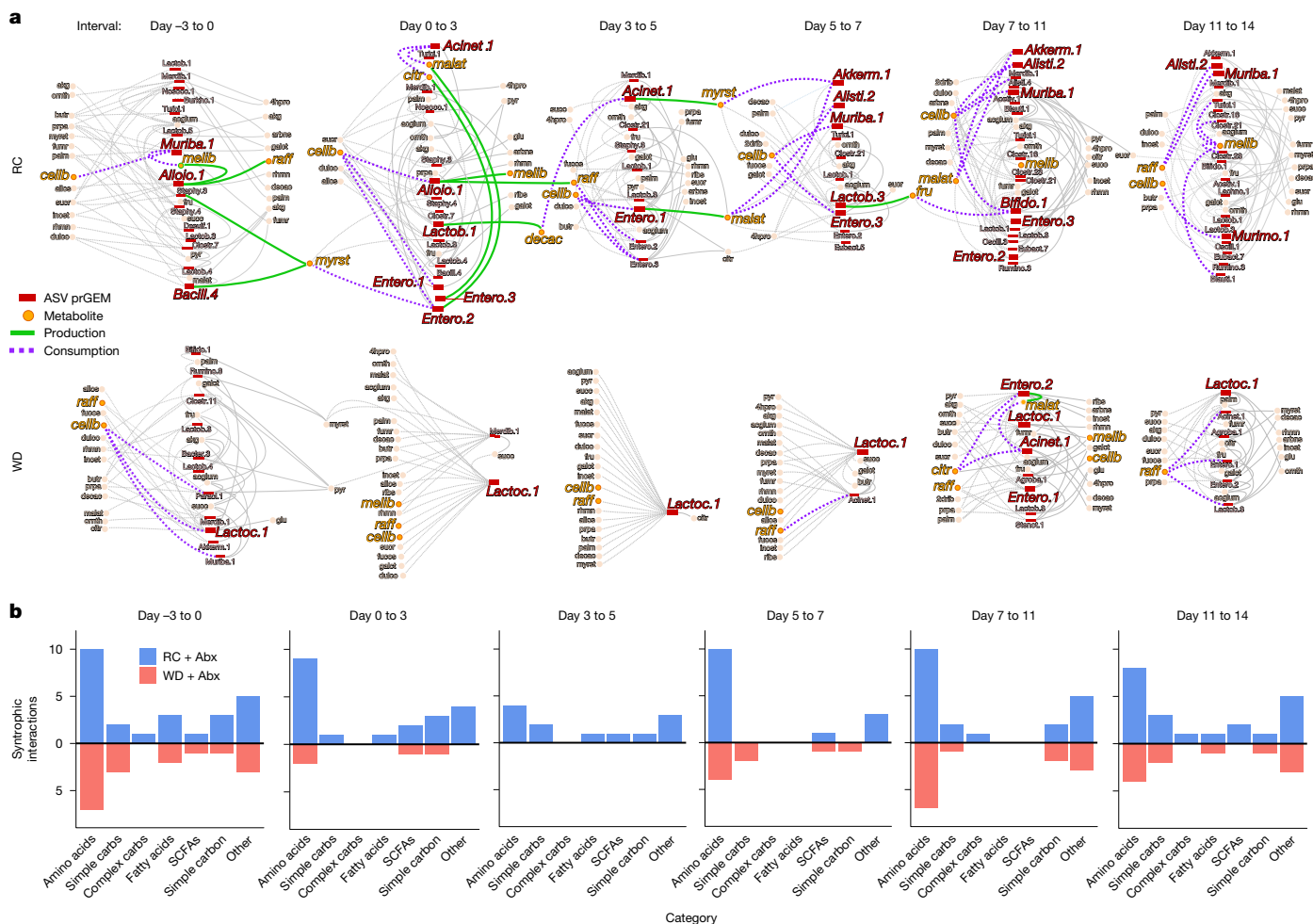


Fig. 3 | Metabolic modelling predicts poor syntrophy in mice on WD.

a, Community flux simulations over each time interval for mice on RC-Abx or WD-Abx. Edges represent predicted flux (dashed, consumption; solid, production) and nodes represent metabolites or ASV prGEMs. Select fluxes predicted to have a crucial role in recovery are highlighted in green and purple; other fluxes are shown in grey. The map includes all measured metabolites with fluxes greater than 0.05 excluding niacin, acetate, propionate and amino acids

for visual clarity, but the full model with all flux values, as well as spelling out of abbreviated metabolite names, is available in Supplementary Table 8. An interactive map with flux values is available at https://modelseed.org/annotation/projects/gut_microbiome/. **b**, Number of syntrophic interactions identified in the community models for mice on RC and WD by category over each time interval. Carbs, carbohydrates.

differences between the RC and WD treatment groups. In the RC communities, ecological complexity and syntrophic cross-feeding interactions are maintained in the immediate aftermath of antibiotic treatment and throughout recovery, resulting in complex, tangled metabolic networks (Fig. 3a,b and Extended Data Fig. 6). By contrast, in WD communities, almost all syntrophic interactions are lost in the aftermath of antibiotic treatment through day 7–11. Instead, the WD communities are dominated by a single Lactococcus ASV with broad metabolic capacity that produces few syntrophic byproducts. The RC community contains this same Lactococcus ASV, but in the RC dietary context, it is balanced by trophic complexity and interdependencies with other strains, so that it never dominates the microbiome. Although amino acids are excluded from Fig. 3a for visual clarity, the observed patterns of greater metabolic interactivity, syntropy and complexity in the RC relative to WD microbiome do also apply to amino acid metabolism (Fig. 3b and Supplementary Table 8).

The community simulations further reveal metabolic succession in the recovery of the RC microbiome. Immediately after antibiotics, flux through oxygen-consuming ASV sets increases for mice on both diets, but more for mice on WD (Extended Data Fig. 6h and Methods). In mice on RC, Muribaculum abundance declines, leaving open a niche for the consumption of cellobiose. This is filled by various facultatively

anaerobic Enterococci, which consume cellobiose and raffinose and produce metabolic products such as citrate and malate, cultivating a niche for aerobic Acinetobacter to emerge. The continued production of malate from Enterococcus and the production of myristate from Acinetobacter open a niche for anaerobic Akkermansia and the anaerobic complex carbohydrate consumers Alistipes and Muribaculum. By day 7–11, Muribaculum has largely replaced Enterococcus as the primary consumer of cellobiose and raffinose, as in the pre-antibiotic state, and aerobic flux has returned to baseline with the emergence of stricter anaerobes. The partial recovery observed in WD mice between day 7–11 also begins with the emergence of Enterococcus. In this dietary context however, they are insufficient to shift the community towards complete recovery, and flux from oxygen-consuming species remains persistently high.

Collectively, our model suggests that metabolism of complex carbohydrates such as cellobiose and raffinose, which are relatively more abundant in RC than in the purified WD, drive the syntrophic interactions that facilitate succession, diversification and recovery. On WD, despite the overlapping taxa of the microbiome and relatively broad capacity to metabolize the same compounds after antibiotics, the greater availability of simple sugars promotes dominance of a single taxon. Thus, dietary resource availability fundamentally shapes the way

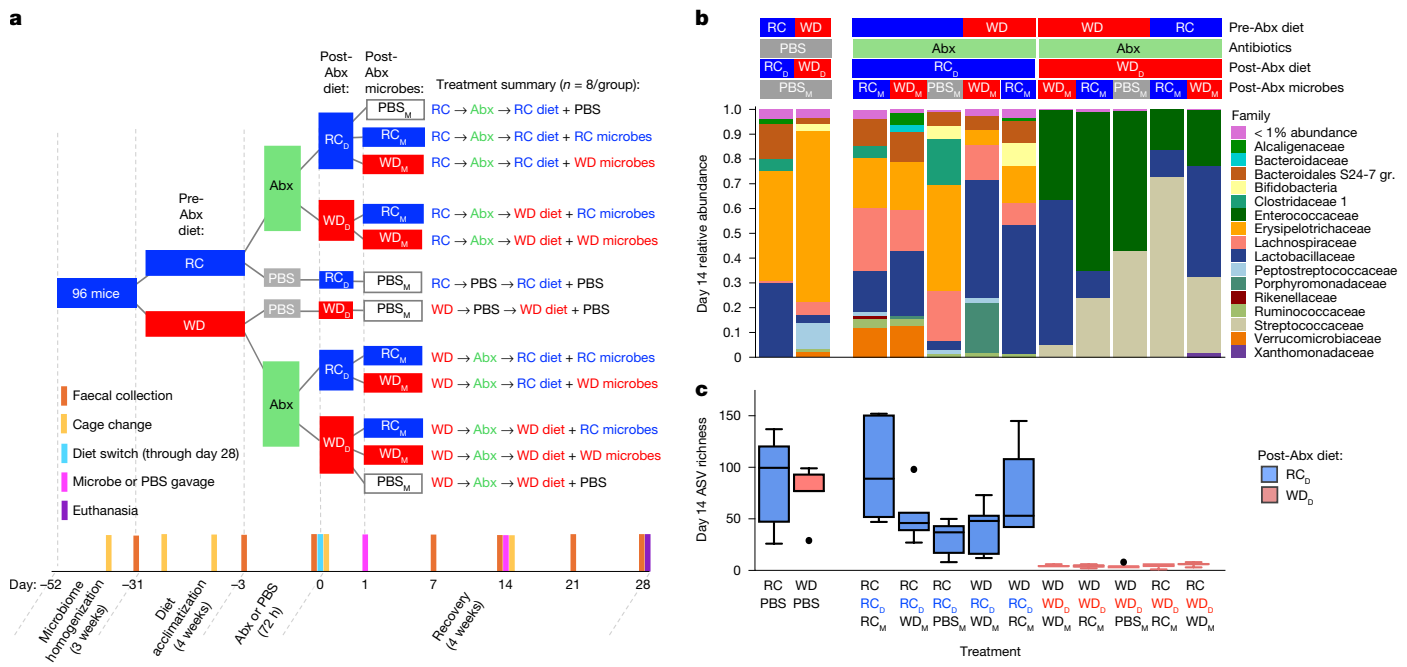


Fig. 4 | Dietary intervention facilitates microbiome recovery from antibiotics. **a**, Experimental design. After Abx or PBS, post-Abx dietary treatments (RC_D and WD_D) were provided ad libitum from day 0 until the end of the experiment; post-Abx microbial treatments (RC_M, WD_M and PBS_M) were administered at day 1 and day 14. **b**, Mean relative abundances of microbial families at day 14 across treatment groups (RC-PBS-PBS: $n = 6$ mice; WD-PBS-PBS: $n = 7$; RC-RC_D-RC_M: $n = 6$; RC-RC_D-WD_M: $n = 7$; RC-RC_D-PBS_M: $n = 7$).

WD-RC_D-WD_M: $n = 7$; WD-RC_D-RC_M: $n = 7$; WD-WD_D-RC_M: $n = 6$; WD-WD_D-PBS_M: $n = 7$; RC-WD_D-RC_M: $n = 6$; RC-WD_D-WD_M: $n = 6$. Gr., group. **c**, ASV richness across treatment groups at day 14 (n values as in **b**). In box plots, the centre line is the median, the top and bottom hinges reflect the first and third quartiles, respectively, and the whiskers extend to 1.5 times the interquartile range. Data beyond the whiskers are plotted as individual points. Statistics, including exact P values, are presented in Supplementary Table 9.

that available taxa interact with their environment and other microorganisms to promote or prevent recovery.

Dietary intervention versus FMT

Our data suggest that recovery in WD is limited primarily by an imbalance in the availability of simple and complex carbohydrates rather than lack of metabolically capable taxa. To test this, we performed intervention experiments in which diet and microbial re-exposures were controlled after antibiotic treatment (Fig. 4a and Methods). In brief, after antibiotic treatment, mice on each pre-antibiotic diet were transferred into sterile gnotobiotic cages, and different post-antibiotic diet (RC_D and WD_D) and microbial re-exposures (RC_M and WD_M) were administered in a factorial manner. Microbial re-exposure was administered via FMT at 24 h post-antibiotics and again at day 14; one group on each diet received sterile PBS_M gavage as a no-transplant control. Faecal samples were collected before and after antibiotic treatment, and weekly up to day 28 of recovery. We selected day 14 as the most salient timepoint to evaluate the distinct recovery dynamics of mice on RC and WD (full time-course data are available in Extended Data Fig. 7 and Supplementary Discussion). No-Abx controls on each diet serve as benchmarks for ‘recovery’, which was evaluated in terms of overall community composition via 16S rRNA sequencing (Fig. 4b) and further quantified by PCOA clustering analysis (Extended Data Fig. 7 and Supplementary Table 9) and ASV richness (Fig. 4c and Supplementary Table 9).

We first confirmed that this experimental model recapitulates the phenotypes of our original experiments: mice that did not change dietary or microbial re-exposures (RC → RC_D or RC_M and WD → WD_D or WD_M) matched the RC-Abx and WD-Abx phenotypes described in Fig. 1. From relative abundance plots, we see that irrespective of pre-Abx diet or post-Abx microbial transplant, gut microbiota composition broadly segregates on the basis of post-Abx diet (Fig. 4b). PCOA confirms that

gut microbial composition segregates across PC1 by post-Abx diet, with mice on RC_D uniformly falling lower on PC1 and closer to the no-Abx controls than mice on WD_D (Extended Data Fig. 7 and Supplementary Table 9). Similarly, mice on post-Abx RC_D uniformly recovered more ASV richness by day 14 than all WD_D counterparts (Fig. 4c and Supplementary Table 9).

Among mice that were fed post-Abx WD_D, microbial transplant had negligible impact on recovery, with all WD_D treatment groups exhibiting severely diminished ASV richness and clustering distinctly from WD no-Abx controls at day 14. These experiments indicate that an appropriate diet is both necessary and sufficient for rapid and robust gut microbiota recovery after antibiotic treatment, whereas microbial transplant is neither. This supports our modelling predictions that recovery is predominantly driven by dietary resource availability (especially the balance of simple and complex carbohydrates) rather than by the presence or absence of specific taxa.

Loss of colonization resistance

Under healthy conditions, the microbiome protects the host via ‘colonization resistance’ against opportunistic pathogens¹⁵. For example, the pathogen *S. enterica* serovar Typhimurium (ST) is unable to establish lower gastrointestinal tract infection or cause colitis in SPF mice unless they have been pre-treated with streptomycin¹⁶. However, established models of ST colonization resistance evaluated susceptibility to infection at only 24 h after antibiotic pre-treatment. We hypothesized that the prolonged post-antibiotic dysbiosis experienced by mice on WD might render them more susceptible to infection by ST as late as 14 days after antibiotic treatment.

To evaluate this possibility, we performed a series of experiments that included five cohorts of female mice and one cohort of male mice (Methods). After antibiotic or PBS administration, mice recovered

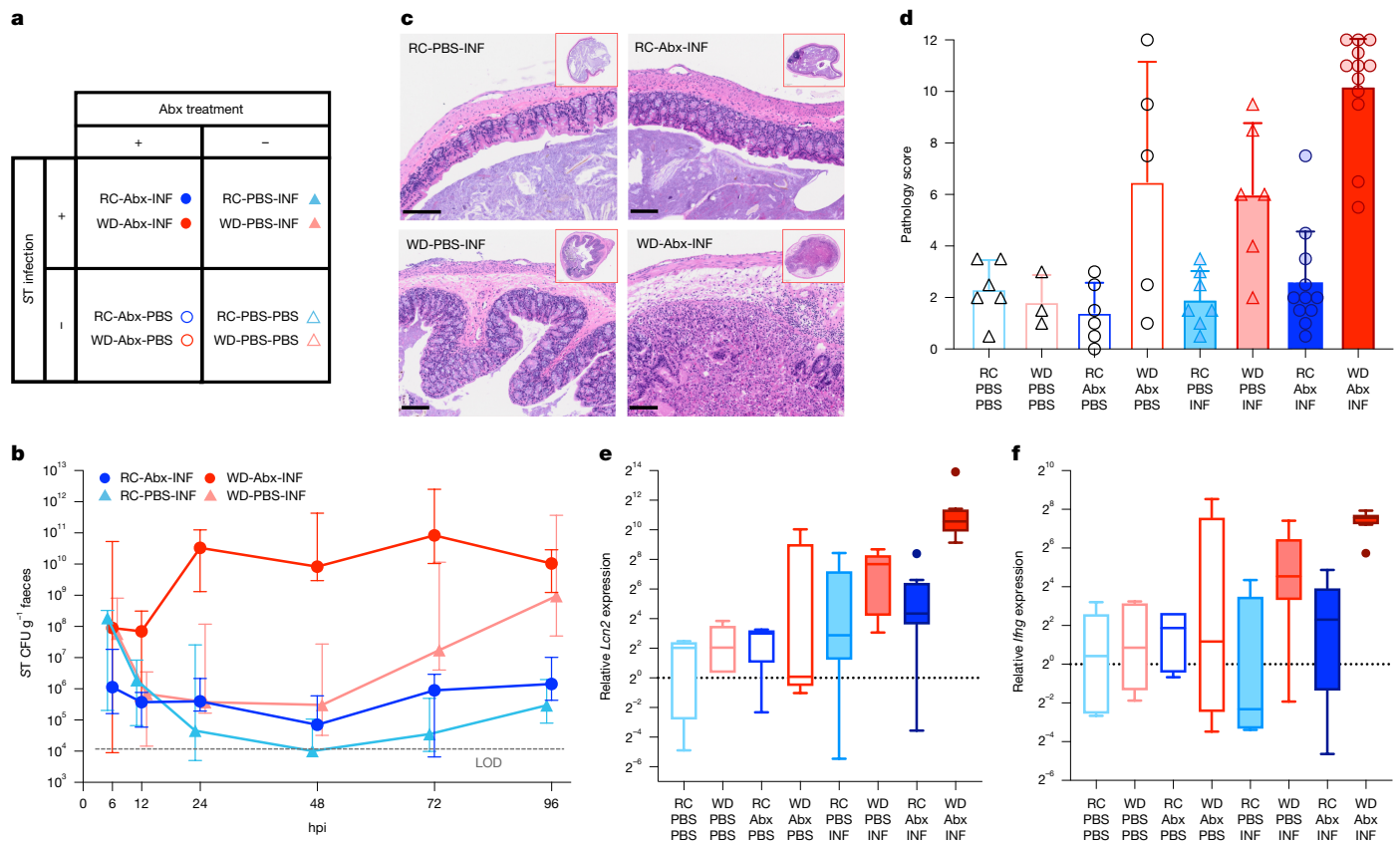


Fig. 5 | Prolonged post-antibiotic dysbiosis in mice on WD impairs colonization resistance to ST. As trends were consistent across male and female cohorts (Extended Data Fig. 8), data were combined to improve statistical power. **a**, Experimental treatment groups. **b**, Faecal ST load among infected treatment groups. Uninfected controls had no detectable ST and are not depicted. Data are median \pm 1.5 \times interquartile range. $n = 6$ to 13 mice per treatment per timepoint; statistics, including exact n and P values, are presented in Supplementary Table 10. **c,d**, Representative histology (**c**) and corresponding histopathological scoring (**d**) of caecal sections from mice on indicated treatment groups at 96 hpi (RC-PBS-PBS: $n = 6$; WD-PBS-PBS: $n = 3$; RC-Abx-PBS: $n = 6$; WD-Abx-PBS: $n = 5$; RC-PBS-INF: $n = 7$; WD-PBS-INF: $n = 6$; RC-Abx-INF: $n = 11$; WD-Abx-INF: $n = 12$; Extended Data Fig. 8). Data are mean \pm s.d. Statistics, including exact P values, are presented in Supplementary Table 10. Scale bars, 100 μ m. **e,f**, mRNA expression of immune system genes in caecal mucosal scrapings at $t = 96$ hpi, on the basis of PCR with reverse transcription (RT-qPCR) (additional inflammatory markers are shown in Extended Data Fig. 8; RC-PBS-PBS: $n = 5$; WD-PBS-PBS: $n = 6$; RC-Abx-PBS: $n = 4$; WD-Abx-PBS: $n = 5$; RC-PBS-INF: $n = 6$; WD-PBS-INF: $n = 6$; RC-Abx-INF: $n = 11$; WD-Abx-INF: $n = 8$). Expression is normalized to the housekeeping gene *Actb* and the RC-PBS-PBS treatment group. In box plots, the centre line is the median, the top and bottom hinges reflect the first and third quartiles, respectively, and the whiskers extend to 1.5 times the interquartile range. Data beyond the whiskers are plotted as individual points. Statistics, including exact n and P values, are presented in Supplementary Table 10.

including exact P values, are presented in Supplementary Table 10. Scale bars, 100 μ m. **e,f**, mRNA expression of immune system genes in caecal mucosal scrapings at $t = 96$ hpi, on the basis of PCR with reverse transcription (RT-qPCR) (additional inflammatory markers are shown in Extended Data Fig. 8; RC-PBS-PBS: $n = 5$; WD-PBS-PBS: $n = 6$; RC-Abx-PBS: $n = 4$; WD-Abx-PBS: $n = 5$; RC-PBS-INF: $n = 6$; WD-PBS-INF: $n = 6$; RC-Abx-INF: $n = 11$; WD-Abx-INF: $n = 8$). Expression is normalized to the housekeeping gene *Actb* and the RC-PBS-PBS treatment group. In box plots, the centre line is the median, the top and bottom hinges reflect the first and third quartiles, respectively, and the whiskers extend to 1.5 times the interquartile range. Data beyond the whiskers are plotted as individual points. Statistics, including exact n and P values, are presented in Supplementary Table 10.

for 14 days, and then each dietary and antibiotic treatment group was split into infection (INF) and no-infection (PBS) treatment groups (Fig. 5a). WD has been shown to facilitate ST infection relative to RC even without antibiotic pre-treatment¹⁷; by comparing Abx and no-Abx control groups on each diet, we isolated the specific effects of diet versus diet-induced post-antibiotic dysbiosis. Faecal samples and body weights were collected up to 96 hours post-infection (hpi).

We first evaluated ST load at each timepoint after infection (Fig. 5b). Uninfected controls had undetectable levels of ST, confirming no contamination. As hypothesized, WD-Abx-INF mice were the most susceptible to infection, exhibiting significantly higher ST loads than all other treatment groups from $t = 24$ –48 hpi and reaching around 10⁵-fold higher median infection load than the WD-PBS-INF group during this period (Supplementary Table 10). From 72–96 hpi, both the WD-Abx-INF and WD-PBS-INF groups had significantly greater infection load than all groups on RC diet, recapitulating previous findings that WD alone is sufficient to impair colonization resistance. Although the WD-Abx-INF group had greater median ST load than WD-PBS-INF up to 96 hpi, this difference was no longer significant after 48 hpi.

We performed targeted analyses of infection severity in lower gastrointestinal tissues to focus on the enteric colonization resistance (rather than disseminated typhoid) model of ST infection^{16,18} (gross

body weight data are available in Extended Data Fig. 8 and Supplementary Discussion). Histopathological scoring and quantitative PCR (qPCR) analysis of a panel of ST-induced inflammatory markers in caecal tissue revealed that the WD-Abx-INF group experienced significantly more severe inflammatory pathology (Fig. 5c,d) with higher expression of inflammatory markers (Fig. 5e,f, Extended Data Fig. 8 and Supplementary Table 10) than all other treatment groups. Notably, the uninfected WD-Abx-PBS control group experienced variable but occasionally severe inflammation resembling the WD-Abx-INF group, suggesting that antibiotic treatment in mice on WD can induce inflammation even without ST challenge. However, only the WD-Abx-INF group consistently succumbed to lower gastrointestinal tract infection and enteritis, supporting the hypothesis that prolonged post-antibiotic dysbiosis in mice on WD impairs colonization resistance in the lower gastrointestinal tract.

Discussion

A fragmented body of work has begun to outline the mechanism by which complex carbohydrates and fibre sources promote microbiome recovery. Our work represents a translationally important integration and extension of these concepts within one *in vivo* system. We

Article

recapitulate the importance of fibre for microbiome recovery after antibiotics as previously shown in mice on an otherwise low-fat diet^{19–21}, but document even more severe and prolonged dysbiosis in the context of a clinically relevant Western-style diet with both low fibre and high fat content. We reaffirm that complex carbohydrates promote the development of syntrophy and community complexity as previously shown with defined microbial consortia *in vitro*^{22,23}, but demonstrate this effect within a complex, endogenous *in vivo* ecosystem. We look beyond the initial redox and metagenomic perturbations in the aftermath of antibiotic treatment^{19,21,24–26} with a novel metabolic modelling approach that predicts the diet-driven successional dynamics that mediate recovery. Together, we arrive at a unified model in which the absence of fibre leads to profound redox imbalance after antibiotic treatment, which is probably exacerbated by the increased production of reactive oxygen species under the high-fat conditions of WD^{27–29}. This promotes the growth of facultatively aerobic organisms^{19,24,30,31} that prioritize the use of fats and simple sugars over complex carbohydrates. Without the breakdown of complex carbohydrates, the community is unable to open up niche space and diversify via syntrophic, facilitative interactions. Explicit quantification of the contributions of fibre and fat to these processes requires further experimentation.

Given the increasing global consumption of Western-style diets³² and liberal use and misuse of antibiotics³³, our findings bear great clinical relevance. In humans, variability in microbiome recovery after antibiotics is well documented, but poorly understood^{30,34,35}. Our data suggest that diet may have a central role in driving inter-individual differences in microbiome recovery and should be explicitly assessed in human studies. Some aspects of our results, such as the early predominance of facultative anaerobes^{30,31} and the impairment of overall microbiome recovery in zero-fibre diets⁸, have indeed been demonstrated in humans. We therefore expect that our broader conclusions about the effect of diet on post-antibiotic recovery and the efficacy of microbial transplant will be conserved across host systems, and moreover, that these dynamics will be largely explainable by microbial metabolic interactions.

Our results also underscore the substantial risks of prolonged post-antibiotic dysbiosis, particularly for populations that are vulnerable to opportunistic infection. Although microbiome dysbiosis due to insults such as antibiotic treatment^{16,36}, bowel prep regimens³⁷ or diarrhoeal illness³⁸ has been shown to promote opportunistic infection immediately following the perturbation, our work suggests that dietary conditions can considerably extend the window of susceptibility. Peri-antibiotic dietary interventions should be investigated across clinical contexts as a safe and affordable route to promote microbiome recovery when iatrogenic collateral damage to the microbiome is unavoidable.

Thus far, the growing field of microbiome therapeutics has centred largely on microbial replacement strategies such as FMT³⁹, probiotics⁴⁰ or live biotherapeutics⁴¹, which have shown variable efficacy across individuals and diseases. Notably, few human studies thus far have explicitly evaluated the effect of recipient diet on the success of microbial transplant, and the vast majority did not even report recipient dietary information^{42,43}. Our intervention experiments indicate that diet is more foundational to recovery than microbial re-seeding, and that without an appropriate dietary resource environment, microbial transplant is insufficient to promote recovery. In contexts with more significant microbial extinction than in our experiments, microbial replacement may yet have an important role in recovery, as has been extensively shown^{7,9,10}. However, our data suggest that unless the microbial transplant encounters an environment with the resources to support engraftment, growth and diversification, its efficacy will be limited at best. Thus, adjunctive dietary interventions may improve the consistency and efficacy of existing microbial transplant strategies.

Finally, we propose ecological succession as a novel paradigm for approaching microbiome restoration. Under this model, both the taxa present and their surrounding resource environment interact

in an iterative feedback process to guide the progression of community development^{44,45}. Early-arriving microorganisms may facilitate or inhibit the growth of later-arriving microorganisms by producing metabolic byproducts for cross-feeding⁴⁶ or by changing the resource environment (for example, oxygen levels⁴⁷, pH⁴⁸ and bile acid pool⁴⁹). The community cannot proceed to the next stage if it is either missing the right taxa, or if the taxa do not have access to the right resources. Our data and simulations indicate that WD does not provide the right balance of simple and complex carbohydrates to initiate this successional process even when the right taxa are present. In this sense, FMT in mice on WD is akin to transplanting a mature forest into barren soil after a fire: the soil is unable to accommodate its growth. By using approaches such as the metabolic model presented here, we can resolve the transitional dynamics between healthy and disease states and learn to support succession at each stage by matching specific dietary or microbial interventions to the present needs of the community. In this way, we can promote the environmental change that is necessary to once again accommodate the growth of the climax community.

Online content

Any methods, additional references, Nature Portfolio reporting summaries, source data, extended data, supplementary information, acknowledgements, peer review information; details of author contributions and competing interests; and statements of data and code availability are available at <https://doi.org/10.1038/s41586-025-08937-9>.

1. Bisanz, J. E., Upadhyay, V., Turnbaugh, J. A., Ly, K. & Turnbaugh, P. J. Meta-analysis reveals reproducible gut microbiome alterations in response to a high-fat diet. *Cell Host Microbe* **26**, 265–272.e4 (2019).
2. Sonnenburg, E. D. & Sonnenburg, J. L. Starving our microbial self: the deleterious consequences of a diet deficient in microbiota-accessible carbohydrates. *Cell Metab.* **20**, 779–786 (2014).
3. Nieuwdorp, M., Giljumse, P. W., Pai, N. & Kaplan, L. M. Role of the microbiome in energy regulation and metabolism. *Gastroenterology* **146**, 1525–1533 (2014).
4. Asnicar, F. et al. Microbiome connections with host metabolism and habitual diet from 1,098 deeply phenotyped individuals. *Nat. Med.* **27**, 321–332 (2021).
5. Turnbaugh, P. J. et al. An obesity-associated gut microbiome with increased capacity for energy harvest. *Nature* **444**, 1027–1131 (2006).
6. Levy, M., Kolodziejczyk, A. A., Thaiss, C. A. & Elinav, E. Dysbiosis and the immune system. *Nat. Rev. Immunol.* **17**, 219–232 (2017).
7. Ng, K. M. et al. Recovery of the gut microbiota after antibiotics depends on host diet, community context, and environmental reservoirs. *Cell Host Microbe* **26**, 650–665.e4 (2019).
8. Tanes, C. et al. Role of dietary fiber in the recovery of the human gut microbiome and its metabolome. *Cell Host Microbe* **29**, 394–407.e5 (2021).
9. Taur, Y. et al. Reconstitution of the gut microbiota of antibiotic-treated patients by autologous fecal microbiota transplant. *Sci. Transl. Med.* **10**, eaap9489 (2018).
10. Tropini, C. et al. Transient osmotic perturbation causes long-term alteration to the gut microbiota. *Cell* **173**, 1742–1754.e17 (2018).
11. Shade, A. et al. Fundamentals of microbial community resistance and resilience. *Front. Microbiol.* **3**, 417 (2012).
12. May, R. M. Will a large complex system be stable? *Nature* **238**, 413–414 (1972).
13. Kennedy, M. S. et al. Dynamic genetic adaptation of *Bacteroides thetaiotaomicron* during murine gut colonization. *Cell Rep.* **42**, 113009 (2023).
14. Faria, J. P. et al. ModelSEED v2: High-throughput genome-scale metabolic model reconstruction with enhanced energy biosynthesis pathway prediction. Preprint at [bioRxiv https://doi.org/10.1101/2023.10.04.556561](https://doi.org/10.1101/2023.10.04.556561) (2023).
15. Buffie, C. G. & Pamer, E. G. Microbiota-mediated colonization resistance against intestinal pathogens. *Nat. Rev. Immunol.* **13**, 790–801 (2013).
16. Barthel, M. et al. Pretreatment of mice with streptomycin provides a *Salmonella enterica* serovar *Typhimurium* colitis model that allows analysis of both pathogen and host. *Infect. Immun.* **71**, 2839 (2003).
17. Wotzka, S. Y. et al. *Escherichia coli* limits *Salmonella Typhimurium* infections after diet shifts and fat-mediated microbiota perturbation in mice. *Nat. Microbiol.* **4**, 2164–2174 (2019).
18. Santos, R. L. et al. Animal models of *Salmonella* infections: enteritis versus typhoid fever. *Microbes Infect.* **3**, 1335–1344 (2001).
19. Penumatchu, S., Korry, B. J., Hewlett, K. & Belenky, P. Fiber supplementation protects from antibiotic-induced gut microbiome dysbiosis by modulating gut redox potential. *Nat. Commun.* **14**, 5161 (2023).
20. Costa, S. K. et al. Short-term dietary intervention with whole oats protects from antibiotic-induced dysbiosis. *Microbiol. Spectr.* **11**, e02376-23 (2023).
21. Xu, R. et al. Pectin supplementation accelerates post-antibiotic gut microbiome reconstitution orchestrated with reduced gut redox potential. *ISME J.* **18**, wrae101 (2024).
22. Ostrem Loss, E., Thompson, J., Cheung, P. L. K., Qian, Y. & Venturelli, O. S. Carbohydrate complexity limits microbial growth and reduces the sensitivity of human gut communities to perturbations. *Nat. Ecol. Evol.* **7**, 127–142 (2023).

23. Yao, T., Chen, M.-H. & Lindemann, S. R. Structurally complex carbohydrates maintain diversity in gut-derived microbial consortia under high dilution pressure. *FEMS Microbiol. Ecol.* **96**, fiaa158 (2020).
24. Reese, A. T. et al. Antibiotic-induced changes in the microbiota disrupt redox dynamics in the gut. *eLife* **7**, e35987 (2018).
25. Cabral, D. J., Wurster, J. I., Korry, B. J., Penumutchu, S. & Belenky, P. Consumption of a Western-style diet modulates the response of the murine gut microbiome to ciprofloxacin. *mSystems* **5**, e00317–e00320 (2020).
26. Lee, J. Y. et al. High-fat diet and antibiotics cooperatively impair mitochondrial bioenergetics to trigger dysbiosis that exacerbates pre-inflammatory bowel disease. *Cell Host Microbe* **28**, 273–284.e6 (2020).
27. Qiao, Y., Sun, J., Ding, Y., Le, G. & Shi, Y. Alterations of the gut microbiota in high-fat diet mice is strongly linked to oxidative stress. *Appl. Microbiol. Biotechnol.* **97**, 1689–1697 (2013).
28. Cui, J., Le, G., Yang, R. & Shi, Y. Lipoic acid attenuates high fat diet-induced chronic oxidative stress and immunosuppression in mice jejunum: a microarray analysis. *Cell. Immunol.* **260**, 44–50 (2009).
29. Li, X. et al. High-fat diet promotes experimental colitis by inducing oxidative stress in the colon. *Am. J. Physiol.* **317**, G453–G462 (2019).
30. Palleja, A. et al. Recovery of gut microbiota of healthy adults following antibiotic exposure. *Nat. Microbiol.* **3**, 1255–1265 (2018).
31. Dubinsky, V. et al. Predominantly antibiotic-resistant intestinal microbiome persists in patients with pouchitis who respond to antibiotic therapy. *Gastroenterology* **158**, 610–624.e13 (2020).
32. *What We Eat in America: Nutrient Intakes from Food by Gender and Age—National Health and Nutrition Examination Survey Data* (US Centers for Disease Control and Prevention, 2009).
33. Wang, J., Wang, P., Wang, X., Zheng, Y. & Xiao, Y. Use and prescription of antibiotics in primary health care settings in China. *JAMA Int. Med.* **174**, 1914–1920 (2014).
34. Dethlefsen, L. & Relman, D. A. Incomplete recovery and individualized responses of the human distal gut microbiota to repeated antibiotic perturbation. *Proc. Natl Acad. Sci. USA* **108**, 4554–4561 (2011).
35. Zaura, E. et al. Same exposure but two radically different responses to antibiotics: resilience of the salivary microbiome versus long-term microbial shifts in feces. *mBio* **6**, e01693–15 (2015).
36. Jenior, M. L., Leslie, J. L., Young, V. B. & Schloss, P. D. *Clostridium difficile* colonizes alternative nutrient niches during infection across distinct murine gut microbiomes. *mSystems* **2**, e00063–17 (2017).
37. Tomkovich, S. et al. An osmotic laxative renders mice susceptible to prolonged *Clostridioides difficile* colonization and hinders clearance. *mSphere* **6**, e0062921 (2021).
38. VanInsberghe, D. et al. Diarrhoeal events can trigger long-term *Clostridium difficile* colonization with recurrent blooms. *Nat. Microbiol.* **5**, 642–650 (2020).
39. Cohen, N. A. & Mahershak, N. Novel Indications for fecal microbial transplantation: update and review of the literature. *Dig. Dis. Sci.* **62**, 1131–1145 (2017).
40. Ritchie, M. L. & Romanuk, T. N. A meta-analysis of probiotic efficacy for gastrointestinal diseases. *PLoS ONE* **7**, e34938 (2012).
41. O'Toole, P. W., Marchesi, J. R. & Hill, C. Next-generation probiotics: the spectrum from probiotics to live biotherapeutics. *Nat. Microbiol.* **2**, 17057 (2017).
42. Porcari, S. et al. Key determinants of success in fecal microbiota transplantation: from microbiome to clinic. *Cell Host Microbe* **31**, 712–733 (2023).
43. Danne, C., Rolhion, N. & Sokol, H. Recipient factors in faecal microbiota transplantation: one stool does not fit all. *Nat. Rev. Gastroenterol. Hepatol.* **18**, 503–513 (2021).
44. Gilbert, J. A. & Lynch, S. V. Community ecology as a framework for human microbiome research. *Nat. Med.* **25**, 884–889 (2019).
45. Prach, K. & Walker, L. R. Four opportunities for studies of ecological succession. *Trends Ecol. Evol.* **26**, 119–123 (2011).
46. Douglas, A. E. The microbial exometabolome: ecological resource and architect of microbial communities. *Phil. Trans. R. Soc. B* **375**, 20190250 (2020).
47. Lee, J.-Y., Tsolis, R. M. & Bäumler, A. J. The microbiome and gut homeostasis. *Science* **377**, eabpp9960 (2022).
48. Van Herreweghen, F., De Paepe, K., Roume, H., Kerckhof, F.-M. & Van de Wiele, T. Mucin degradation niche as a driver of microbiome composition and *Akkermansia muciniphila* abundance in a dynamic gut model is donor independent. *FEMS Microbiol. Ecol.* **94**, fiy186 (2018).
49. Ridlon, J. M., Kang, D. J., Hylemon, P. B. & Bajaj, J. S. Bile acids and the gut microbiome. *Curr. Opin. Gastroenterol.* **30**, 332–338 (2014).

Publisher's note Springer Nature remains neutral with regard to jurisdictional claims in published maps and institutional affiliations.

Springer Nature or its licensor (e.g. a society or other partner) holds exclusive rights to this article under a publishing agreement with the author(s) or other rightsholder(s); author self-archiving of the accepted manuscript version of this article is solely governed by the terms of such publishing agreement and applicable law.

© The Author(s), under exclusive licence to Springer Nature Limited 2025

Article

Methods

Mice

C57BL/6 mice at 5 weeks of age were purchased from The Jackson Laboratory barrier facility EM04 and co-housed in cages of 2–4 mice with pine shavings bedding in standard barrier facilities unless otherwise specified. Facilities maintained a 12 h:12 h light-dark cycle with lights on at 06:00 and lights off at 18:00. Temperatures were maintained between 20 °C and 21 °C, and humidity was kept between 30% and 70%. All mice underwent a two-step microbiome homogenization protocol: (1) bedding was mixed across all cages twice a week from age 5–8 weeks leading up to the beginning of each experiment to reduce intra-cohort cage effects; and (2) mice were gavaged once at 6 weeks with faecal material banked from our SPF colony to reduce inter-cohort differences in microbiome composition⁵⁰. We chose to use conventionally raised mice with an endogenous mouse microbiome rather than a humanized mouse model since published data indicates that human taxa are less able to engraft in mouse gut ecosystems, even when the mice are germ-free^{51–53}. Since many of our experiments explicitly sought to quantify diversity before and after antibiotics, and since community recovery dynamics may rely substantially on functional redundancy among community members⁵⁴, it was essential to use a model with a sufficiently complex, natural microbiota. Mice were fed autoclaved standard RC diet (LabDiets 5K67) during microbiome homogenization. Most experiments used only female mice to minimize variability introduced by sex, but one male cohort was included to ensure that phenotypes were consistent across sexes. This cohort was formally part of the colonization resistance experiment, which underwent an identical protocol to all other experiments through day 14 of recovery.

Diet acclimatization and antibiotic treatment

Mice at 8 weeks of age were either maintained on RC diet (LabDiets 5K67, 22.4% kcals from protein, 62.0% from carbohydrate, 15.6% from fat, 154 g fibre per kg) or switched to WD (Envigo TD.97222, 15.8% kcal from protein, 46.8% from carbohydrate, 37.4% from fat, 45 g fibre per kg)⁵⁵ to acclimate for 4 weeks. While our RC diet reflects a standard, fibre-rich mouse chow derived from a variety of plant products, including whole wheat, wheat middlings, ground corn, ground oats, dehulled soybean meal, and alfalfa meal, our WD was designed to broadly reflect American nutritional habits on the basis of the Center for Disease Control and Prevention's National Health and Nutrition Examination Survey⁵². This is a purified diet with minimal fibre (cellulose), abundant simple sugars (sucrose), and high fat (derived from milk). During diet acclimatization, bedding was mixed across cages within diet treatments twice a week. At 12 weeks of age, mice on each diet were treated with a sterile-filtered triple antibiotic cocktail of vancomycin (0.5 mg ml⁻¹), neomycin (1.0 mg ml⁻¹), and cefoperazone (0.5 mg ml⁻¹) or 5% sterile PBS control in the drinking water for 72 h. Water consumption was monitored during this time to ensure adequate treatment (Extended Data Fig. 1a).

WD microbiome resilience experiments

Three cohorts of female mice were used in these experiments (including the long-term cohort described below). After treatment with antibiotics or PBS control, mice were maintained on their respective pre-antibiotic diets, and faecal samples were collected for 4 weeks after cessation of antibiotics on days −31, −3, 0, 1–8, 11, 14, 16, 18, 21, 23, 25, and 28. Cages were changed on days −38, −24, −10, 7, and 21. Subsets of mice were euthanized at the pre-antibiotic (day −3), post-antibiotic (day 0), week two of recovery (day 14), or week four of recovery (day 28) timepoints (total $n = 4$ per timepoint per treatment group).

Long-term recovery from WD cohort. One cohort of 8-week old female C57BL/6 mice ($n = 6$ per group, RC-Abx and WD-Abx only) was bred in our animal facility for this experiment. Mice were co-housed in cages of 3 mice with pine shavings bedding in standard barrier facilities and

did not undergo the microbiome homogenization protocol. These mice were acclimated to their respective dietary treatment for only 10 days. Although 10 days of diet acclimatization was predicted to be sufficient for microbiome stabilization⁵⁶, which can occur within 4 days, we extended the diet acclimatization phase in subsequent cohorts to ensure that host physiological differences across dietary groups had stabilized⁵⁷. During diet acclimatization, bedding was mixed across cages within diet treatments twice a week. Antibiotic treatment was administered as described above. Faecal samples were collected for 9 weeks after cessation of antibiotics on days −31, −3, 0, 0.5, 1, 1.5, 2–8, 11, 14, 16, 18, 21, 28, 35, 49, and 63, and then all mice were euthanized. Cage changes were performed on days −10, 7, 21, 35, and 49. Experimental duration was decreased after this cohort as microbiome recovery appeared to stabilize by day 28 (Extended Data Fig. 1).

Post-antibiotic intervention experiments

Four cohorts of female mice were used in these experiments ($n = 8$ per treatment group, $n = 96$ total). For each cohort, 24 mice at 5 weeks of age were split across 4 cages ($n = 6$ per cage) in standard barrier facilities for 3 weeks of microbiome homogenization. After microbiome homogenization, mice were transferred into 8 hermetically sealed gnotobiotic Techniplast IsoCage P Bioexclusion cages for diet acclimatization and antibiotic treatment as described above ($n = 3$ per cage). Immediately following antibiotic treatment (day 0), mice were transferred into 12 new sterile gnotobiotic cages and post-antibiotic diet and microbial re-exposure treatments were administered ($n = 2$ per treatment group per cohort). For microbial re-exposure treatments, faecal material was collected from all mice on the day before antibiotic treatment (day −1), pooled by dietary treatment, resuspended at 60 mg ml⁻¹ in 25% glycerol solution, and frozen at −80 °C until administration. Microbial re-exposures were administered by oral gavage of 200 µl of the respective faecal solution or sterile PBS at 24 h after cessation of antibiotics (day 1) and were re-administered at day 14 of recovery after cage changes were performed to ensure that dispersal limitation did not impair microbiome recovery. Faecal samples were collected on days −31, −3, 0, 7, 14, 21, and 28, and mice were euthanized at day 28 post-Abx.

All procedures on the IsoCage P rack system from the time of antibiotic administration onward were performed using a modified sterile technique necessitated by the logistics of handling such a large number of treatment groups: one researcher donned sterile garb, including two pairs of sterile gloves, the workspace was covered with a sterile drape, and another team member assisted in manipulation of the outside of the cages. The sterile team member performed all mouse manipulations without making contact with anything outside of the cage or sterile field. In between treatment groups, the sterile team member donned new sterile gloves, but otherwise continued to use the same garb. Throughout this experiment, all RC diet was autoclaved and all WD diet was irradiated and tested via microbial culture and PCR to ensure sterility.

Colonization resistance experiments

After diet acclimatization and antibiotic or PBS administration, 4 cohorts of female mice ($n = 3$ –6 per treatment group) and one cohort of male mice ($n = 6$ per treatment group, RC-Abx-INF and WD-Abx-INF only) were allowed to recover for 14 days, and were then inoculated by oral gavage with 200 µl of either nalidixic acid-resistant ST (strain IR715)⁵⁸ or PBS control. To prepare the gavage solution, ST was grown aerobically in Luria broth (LB) media at 30 °C with shaking at 250 rpm for 14 h. Cultures were pelleted by centrifuging for 5 min at 4,000g and resuspended at 1:100 dilution in PBS (final infection dose: 7×10^7 CFU per mouse). Faecal samples and body weights were collected at $t = 6$, 12, 24, 48, 72 and 96 hpi, and then mice were euthanized.

Tissue collection and sample processing

All mice were euthanized by CO₂ asphyxiation and death was confirmed via cervical dislocation. After euthanasia, blood was collected

by cardiac puncture and serum was isolated and stored at -80°C . Liver, spleen, mesenteric lymph nodes, and mesenteric, gonadal, inguinal, and retroperitoneal fat deposits were weighed and split across samples that were preserved for histology, snap-frozen for RNA sequencing, and homogenized for CFU counts. The gastrointestinal tract was dissected out, the caecum was weighed, and colon length was measured. Sections of the ileum, caecum and colon were preserved for histology. Luminal contents from each of these sections were homogenized for CFU counting and snap-frozen for metabolomics or DNA extraction, and mucosal scrapings from each section were snap-frozen for RNA sequencing and/or RT-qPCR.

CFU counts

Pre-weighed faecal samples were suspended in 500 ml of 25% glycerol solution, homogenized for 1 min in a Mini-BeadBeater-96 (no beads, 2,400 rpm), and serially diluted in PBS. Overall bacterial load was quantified by plating on brain heart infusion-supplemented (BHI-S) agar and incubating aerobically and anaerobically at 37°C for 24 h. Measurements of overall bacterial load were collected for the pilot cohort, as well as all colonization resistance experiments. Although we do not have bacterial biomass measurements for the two non-pilot cohorts of the Western diet resilience experiment, the colonization resistance experiments were carried out identically to these experiments through day 14 post-Abx, and data from these timepoints may therefore be interpreted in the same manner. These data, collected from 5 separate cohorts and 48 mice, recapitulate the bacterial biomass dynamics of the RC-Abx and WD-Abx treatment groups reported in Fig. 1b (Extended Data Fig. 1b,c). Moreover, they indicate no significant loss of bacterial biomass over the course of the experiment in RC-PBS or WD-PBS controls.

To evaluate ST load, pre-weighed faecal or tissue samples were homogenized in 25% glycerol solution as described above, and quantified by plating on LB agar with $25\ \mu\text{g ml}^{-1}$ nalidixic acid and incubating at room temperature for 24 h.

DNA extraction

DNA was extracted using the QIAamp PowerFecal Pro DNA kit (Qiagen). Prior to extraction, samples were subjected to mechanical disruption using a bead beating method. In brief, samples were suspended in a bead tube (Qiagen) along with lysis buffer and loaded on a bead mill homogenizer (Fisherbrand). Samples were then centrifuged, and supernatant was resuspended in a reagent that effectively removed inhibitors. DNA was then purified routinely using a spin column filter membrane and quantified using Qubit.

16S rRNA sequencing

The V4–V5 region within the 16S rRNA gene was amplified using universal bacterial primers—563 F (5'-nnnnnnnn-NNNNNNNNNN NN-AYTGGGYDTAAA-GNG-3') and 926 R (5'-nnnnnnnn-NNNNNNNN NNNNN-CCGTCAATTYHT-TTRAGT-3'), where N represents the barcodes and n represents additional nucleotides added to offset primer sequencing. Approximately ~412 bp region amplicons were then purified using a spin column-based method (Qiagen), quantified, and pooled at equimolar concentrations. Illumina sequencing-compatible Unique Dual Index (UDI) adapters were ligated onto the pools using the QIAseq 1-step amplicon library kit (Qiagen). Library quality control was performed using Qubit and Tapestation and sequenced on Illumina MiSeq platform to generate 2×250 -bp reads. Mean read depth was 26,196 reads per sample. Data were analysed with QIIME2 v2022.2 (ref. 59) and the R package phyloseq v1.40.0 (ref. 60), and were visualized with the R package tidyverse v2.0.0 (ref. 61) and GraphPad Prism v10.3.1.

Shotgun metagenomics

Libraries were prepared using 100 ng of genomic DNA using the QIAseq FX DNA library kit (Qiagen). In brief, DNA was fragmented enzymatically

into smaller fragments and desired insert size was achieved by adjusting fragmentation conditions. Fragmented DNA was end repaired and adenine nucleotides were added to the 3' ends to stage inserts for ligation. During ligation step, Illumina-compatible UDI adapters were added to the inserts and the prepared library was amplified by PCR. Amplified libraries were cleaned up, and quality control was performed using a tapestation. Libraries were sequenced on an Illumina NextSeq 500 to generate 2×150 reads. Our co-assembled metagenome had a total contig length of 779,289,202 bp, with mean coverage of 3.43 reads per bp.

Metagenomic analysis

Raw metagenomics reads were trimmed using Trimmomatic⁶², and a Minoche quality filter⁶³ was applied. Reads from all samples were co-assembled using megahit⁶⁴. We then used the anvi'o v7.1 (ref. 65) metagenomic workflow to compute coverage for each gene across metagenomes, and to refine metagenome-assembled-genomes (MAGs). In brief, the workflow uses: (1) Prodigal v2.6.3 (ref. 66) to identify open reading frames (ORFs); (2) anvi-run-hmm to identify single copy core genes from bacteria ($n = 71$) and ribosomal RNAs ($n = 12$) using HMMER v3.3 (ref. 67); (3) anvi-run-pfams, anvi-run-kegg-kofams and anvi-run-cazymes to annotate ORFs with the EBI PFAM database⁶⁸, the KOfam HMM database of KOs⁶⁹, and the dbCAN CAZyme HMM database⁷⁰, respectively. We used Bowtie2 v2.3.5.1 (ref. 71) to recruit metagenomic short reads to the contigs, and samtools v1.11 (ref. 72) to convert SAM files to BAM files. We profiled the resulting BAM files with anvi-profile and used the program anvi-merge to combine all single profiles into a merged profile for downstream visualization. We used anvi-export-gene-coverage-and-detection to generate coverage tables for downstream analysis in R. deseq2 was used on the exported count data to identify differentially abundant KOs across timepoints and treatment groups. For MAG-based analyses, we performed binning with MetaBAT 2 (ref. 73). We created curated lists of all genes involved in the metabolism of several substrates of interest, which were selected because of their presence and dynamics in our metabolomics analysis. First, we used the dbCAN-sub database⁷⁴ to identify genes involved in the metabolism of melibiose/alpha-galactosides, raffinose, starch, xylan, arabinan and cellulose. Using previously published work⁷⁵, we identified a list of genes involved in metabolism of SCFAs. Finally, we collected all genes with KOFams⁷⁶ annotations for metabolism of bile acids. Gene lists are available in Supplementary Table 6. All plots were generated with the R package tidyverse v2.0.0 (ref. 61) or GraphPad Prism v10.3.1 (GraphPad Software).

Metabolite extraction from faecal or caecal material

Metabolites were extracted with the addition of extraction solvent (80% methanol spiked with internal standards and stored at -80°C (Supplementary Table 5)) to pre-weighed faecal or caecal samples at a ratio of 100 mg of material per mL of extraction solvent in beadruptor tubes (Fisherbrand; 15-340-154). Samples were homogenized at 4°C on a Bead Mill 24 Homogenizer (Fisher; 15-340-163), set at $1.6\ \text{m s}^{-1}$ with 6×30 -s cycles, 5 s off per cycle. Samples were then centrifuged at -10°C , 20,000g for 15 min and the supernatant was used for subsequent metabolomic analysis. Caecal samples were used in lieu of faecal samples for SCFA analysis as the caecum is the primary site of SCFA production via fermentation in the gut⁷⁷.

Metabolite analysis using GC-EI-MS and methoxyamine and TMS derivatization

Metabolites were analysed using gas chromatography mass spectrometry with electron impact ionization (GC-EI-MS). To a mass spectrometry autosampler vial (Microliter; 09-1200), 100 μl of metabolite extract was added and dried down completely under a nitrogen stream at $30\ \text{l min}^{-1}$ (top) and $11\ \text{l min}^{-1}$ (bottom) at 30°C (Biotope SPE Dry 96 Dual; 3579 M). To dried samples, 50 μl of freshly prepared $20\ \text{mg ml}^{-1}$ methoxyamine (Sigma; 226904) in pyridine (Sigma; 270970) was added and incubated

Article

in a thermomixer C (Eppendorf) for 90 min at 30 °C and 1,400 rpm. After samples were cooled to room temperature, 80 µl of derivatizing reagent (*N,O*-bis(trimethylsilyl)trifluoroacetamide (BSTFA) + 1% TMCS (trimethylchlorosilane); Sigma B-023) and 70 µl of ethyl acetate (Sigma; 439169) were added and samples were incubated in a thermomixer at 70 °C for 1 h and 1,400 rpm. Samples were cooled to room temperature and 400 µl of ethyl acetate was added to dilute samples. Turbid samples were transferred to microcentrifuge tubes and centrifuged at 4 °C, 20,000g for 15 min. Supernatants were then added to mass spec vials for gas chromatography mass spectrometry analysis. Samples were analysed using a GC-MS (Agilent 7890 A GC system, Agilent 5975 C MS detector) operating in electron impact ionization mode, using a HP-5MSUI column (30 m × 0.25 mm, 0.25 µm; Agilent Technologies 19091S-433UI) and 1 µl injection. Oven ramp parameters: 1 min hold at 60 °C, 16 °C per min up to 300 °C with a 7 min hold at 300 °C. Inlet temperature was 280 °C and transfer line was 300 °C. Data analysis was performed using MassHunter Quantitative Analysis software (version B.10, Agilent Technologies) and confirmed by comparison to authentic standards. Normalized peak areas were calculated by dividing raw peak areas of targeted analytes by averaged raw peak areas of internal standards. Bile acid assays for cholic acid also included allocholic acid; assays for lithocholic acid also included allolithocholic acid and isolithocholic acid.

Histopathology

Caecal tissue cross-sections were fixed with 4% formalin for 24 h and were stored in 70% ethanol until paraffin embedding and tissue sectioning. Embedding, sectioning, and H&E staining were performed by the University of Chicago Human Tissue Resource Center. Each tissue section was scored for pathology in a blinded fashion by a pathologist and a trained researcher according to the system outlined by Barthel et al.¹⁶ In brief, two independent scores for submucosal oedema, polymorphonuclear cell infiltration, goblet cells, and epithelial integrity were averaged for each tissue sample. The combined histopathological score for each sample was determined as the sum of these averaged scores. It ranges between 0 and 12 arbitrary units and covers the following levels of inflammation: 0, no signs of inflammation; 1–2, minimal signs of inflammation; 3–4, slight inflammation; 5–8, moderate inflammation; 9–13, profound inflammation.

RT-qPCR

Total messenger RNA isolated from colonic mucosal scrapings was used with Transcriptor First Strand cDNA Synthesis Kit (Roche Diagnostics Corporation) to obtain cDNA. Real-time qPCR was performed using iTaq Universal SYBR Green Supermix with CFX384 Real-Time System (Bio-Rad). Primers and cycling conditions were derived from Devlin et al.⁷⁸ (Supplementary Table 10). Expression was calculated via $\Delta\Delta C_t$, relative to the housekeeping gene *Actb* and the control group RC-PBS-PBS.

Statistical methods

All statistical information, including specific tests run, sample sizes, test statistics, multiple comparisons, and *P* values, are presented in Supplementary Tables 1–10, organized by experiment. Data processing, figure production, and statistical analysis scripts are available in ref. 79.

Construction of probabilistic annotation from ASV sequences

We mapped as many of the ASV sequences as possible from our amplicon sequencing and analysis pipeline to 16S sequences of full reference genomes that are a part of the AGORA2 set of common gut microorganisms⁸⁰. We selected the AGORA2 set of genomes because it is a curated and quality-controlled set of known mammalian gut microbiome isolates, but we chose not to use their curated models because of technical problems associated with merging individual strain models into pangenome-based model (see Supplementary Methods for more detail). We searched for identical 16S sequences and iteratively reduced

the identity threshold by 1% to 90% until a match was acquired, or if no match was acquired at the 90% threshold, accepted that the ASV does not have a matching AGORA2 genome. We mapped 3,035 distinct AGORA2 reference genomes to 1,654 of the experimentally detected ASVs, and then created 267 ASV sets by grouping ASVs whose reference genomes were all more than 50% identical with each other. The ASV sets were named for the most common genus of each set and appended with a numeric suffix if the genus had already been identified by a previous ASV set (for example, *Lactococcus*.1, then *Lactococcus*.2, and so on), which indicates that the ASV sets embody sub-genus phylogenetic resolution. All mapped reference genomes within an ASV set were loaded into KBase⁷⁹, annotated with RAST⁸¹ (<https://narrative.kbase.us/narrative/178418>), and then all genes with identical RAST annotations were merged into a single functional ‘pseudogene’. A probability p_{func} for each pseudogene in the probabilistic annotation was created from the count of the associated function across the reference genomes of the ASV set divided by the number of reference genomes in the ASV set. These probabilistic annotations were saved in KBase as genome objects (see <https://narrative.kbase.us/narrative/181152>). Each pseudogene was annotated with the corresponding RAST function and the associated probability saved in the evidence score. In the alias list for each pseudogene, we included the full list of gene IDs annotated with the associated RAST function across all the reference genomes comprising the probabilistic annotation. When comparing the function content of our ASV reconstructions to the MAGs assigned to the same taxonomy by GTDBtk, we observed an average overlap of 94.5%, while our ASV reconstructions contained between 336 and 3,448 additional functions not found in the MAGs (Extended Data Fig. 6 and Supplementary Methods).

Reconstruction of prGEM metabolic models based on probabilistic annotations

We applied the MS2-Build Prokaryotic Metabolic Models with OMEGGA app in KBase to reconstruct a draft metabolic model from the probabilistic annotation for each ASV set. Reactions are mapped through this reconstruction process to the probabilistic functional annotations described above. The draft models were gapfilled in glucose minimal media, to ensure that every model includes all the reactions needed to permit growth without any essential auxotrophy, and were further gapfilled on all of our 63 measured metabolites, to ensure that the models were capable of consumption, production, and growth in the metabolic environment determined from our metabolomics data. While many gut microbiota are likely auxotrophic and will not necessarily interact with all our observed metabolites, it is impossible to predict auxotrophy reliably based purely on pangenomes. The gapfilling ensures that all of the pathways needed to interact with the measured metabolites were available and ensures that models can function in diverse contexts that the microbiome environment presents; however, we are not asserting that all ASVs have all of these gapfilled capabilities. All reactions in these ASV set probabilistic genome-scale models (prGEM) are assigned a probability p_{rxn} on the basis of their pseudogene associations. Reactions are assigned the highest p_{func} associated with any of the pseudogenes to which the reaction was matched, while gapfilled reactions are assigned a probability of 0 and are penalized in our optimization as described later. The prGEMs were saved in KBase using the same name as their associated ASV set: <https://narrative.kbase.us/narrative/181152>. To ensure that our ASV sets adequately reflected the functional potential of our communities, we compared the functional annotations of the ASV sets with MAGs derived from our metagenomics data (Supplementary Methods).

Construction of community metabolic models for sample intervals

We created a community prGEM of each interval between experimental samples for which metabolomics data was collected using

the compartmentalized community model formalism described in Henry et al.⁸². The WD and RC treatment groups had slightly different metabolomic sampling points. Specifically, we did not have metabolomics data for days 3 or 5 for mice on WD. Given that the observed metabolite profile underwent minimal change between days 0 and 7 for mice on WD, we re-used the metabolomics data from this interval for our modelling intervals representing days 0–3, 3–5 and 5–7 (Supplementary Table 8a).

The $A_{int, set}$ matrix of ASV set abundances per sample interval is derived from the average of the A_{set} from consecutive timepoints. Interval community models were built for each column in $A_{int, set}$ by merging the ASV set prGEMs with relative abundances >1% into a single probabilistic community model (prcGEM). Each ASV set prGEM compartment was assigned an index, which was appended to the IDs of the transport reactions and the intracellular metabolites and reaction IDs of the contained prGEM, while the exchange fluxes and extracellular metabolite IDs that were shared among all prGEMs have index 0.

The objective function for each prcGEM was defined as follows: one gram of community biomass equals the dot product of the biomass flux and ASV set abundance from the $A_{int, set}$ among all merged prGEMs in the interval. Mathematical formalization of this objective function is presented in the Supplementary Methods. The prcGEM therefore contains the union of ASV sets present in the samples from a given interval, and can capture potential ASV set interactions within the interval. All of these interval-based prcGEMs were saved in KBase (<https://narrative.kbase.us/narrative/181152>).

Simulation of interval community models to predict maximum-likelihood interactions between ASV sets and metabolites

Flux balance analysis simulations of each interval prcGEM predicted the maximum-likelihood interactions between the ASV sets and the measured metabolites in each sample interval. Constraints were adjusted to simulate rich media that includes all compounds that can be utilized by any ASV set in the prcGEM, which reflects both the uncertainty in and complexity of the nutritional environment of the gut microbiome. An upper limit of $300 \left[\frac{C_{atoms}}{gm_{CDW} \times hr} \right]$, where C_{atoms} represents the number of carbon atoms, gm_{CDW} represents grams cell dry weight, or bacterial biomass, and hr represents hours, or timesteps, was placed on the total carbon uptake of the prcGEM to reflect nutrient limitations. All dipeptide exchanges were forced to zero because they add little value for understanding microbiome behaviour yet combinatorially increase complexity compared to simple amino acid exchanges. The total flux of all members (ASV set compartments) were parameterized to be less than 750 times their biomass growth rate, which permits non-auxotrophic optimal growth on glucose in *Escherichia coli* but prevents an ASV from carrying far more flux than is justified by its level of abundance within the microbiome. Oxygen uptake was limited so that full aerobic metabolism would not be possible on maximum carbon consumption, which reflects the gut conditions. The community biomass reaction, with all of the aforementioned constraints, was then maximized and constrained to be at least 50% of this optimal growth to force effective community growth while permitting other specifications of the probabilistic optimization to be met. We attempted to constrain exchange fluxes associated with metabolites with increasing or decreasing concentration over an interval to be positive or negative, respectively, thereby simulating production or consumption of the metabolite by the microbiome. Finally, simulations minimize the dot product of the reaction flux $\nu_{r,i}$ and the inverse probability $(2 - p_{r,i})$ for each reaction $r \in R$ and species (compartment) $i \in I$ for all ASV set prGEMs. This determines the most parsimonious and likely metabolic activity given the metabolic capacity and abundance of each individual ASV set in the community while reproducing some observed metabolite trajectories. To validate our simulations we plotted flux versus biomass growth for all species in all our interval models, demonstrating that all species grew at observed abundances and carried an

approximately proportional amount of flux (Extended Data Fig. 6b,c). Similarly, to test if our simulations reflected our observed metabolomics dynamics, we correlated metabolite exchange fluxes with observed metabolite dynamics, finding that simple carbon, vitamins, and fatty acids displayed the highest correlations at 0.39, 0.31, and 0.15 respectively. An expanded mathematical formalization of this simulation approach is presented in the Supplementary Methods. The resultant community fluxes from simulating these communities were visualized in the Escher map in Fig. 3.

Community oxygen metabolism

To determine the oxygen metabolism of each community, the total O_2 transport flux for each member was first parsed (rxn05468) and normalized to that member's respective biomass growth rate. Next, members whose normalized O_2 transport fluxes were above 2 mmol O_2 per gram of member biomass were classified as significant oxygen consumers. The magnitudes of all reaction fluxes were then summed for each member to calculate total flux for each member. These total fluxes were summed for all members to produce the community-wide total flux. To calculate the percentage of flux through oxygen-consuming organisms, we then summed the total member flux for significant oxygen consumers and divided this by the total community flux (Extended Data Fig. 6h). **Use of experimental animals.** All mouse experiments were conducted in accordance with the University of Chicago Institutional Biosafety Committee and Institutional Animal Care and Use Committee under ACUP 72101.

Reporting summary

Further information on research design is available in the Nature Portfolio Reporting Summary linked to this article.

Data availability

The data, including all DNA sequencing datasets, that support the findings of this study are available in this Article, the supplementary information and BioProject accession PRJNA992061. Metabolomics data have been deposited in the MassIVE database under ID MSV000097318. Other databases used in this work include KEGG⁶⁹, PFAMs⁸³, dbCAN^{70,74}, KOFams⁷⁶, AGORA2⁸⁰ and RAST⁸¹. Source data are provided with this paper.

Code availability

The Jupyter Notebooks in which the modelling data were processed and the figures were developed, as well as scripts for all sequencing data analysis, statistical analysis, and figure production, are accessible at Zenodo (<https://doi.org/10.5281/zenodo.14977112> (ref. 84)).

50. Miyoshi, J. et al. Minimizing confounders and increasing data quality in murine models for studies of the gut microbiome. *PeerJ* **6**, e5166 (2018).
51. Seedorf, H. et al. Bacteria from diverse habitats colonize and compete in the mouse gut. *Cell* **159**, 253–266 (2014).
52. Moeller, A. H. et al. Experimental evidence for adaptation to species-specific gut microbiota in house mice. *mSphere* **4**, e00387–19 (2019).
53. Chung, H. et al. Gut immune maturation depends on colonization with a host-specific microbiota. *Cell* **149**, 1578–1593 (2012).
54. Allesina, S., Bodini, A. & Pascual, M. Functional links and robustness in food webs. *Phil. Trans. R. Soc. B* **364**, 1701–1709 (2009).
55. Howe, A. et al. Divergent responses of viral and bacterial communities in the gut microbiome to dietary disturbances in mice. *ISME J.* **10**, 1217–1227 (2016).
56. Carmody, R. N. et al. Diet dominates host genotype in shaping the murine gut microbiota. *Cell Host Microbe* **17**, 72–84 (2015).
57. Turnbaugh, P. J., Bäckhed, F., Fulton, L. & Gordon, J. I. Diet-induced obesity is linked to marked but reversible alterations in the mouse distal gut microbiome. *Cell Host Microbe* **3**, 213–223 (2008).
58. Diaz-Ochoa, V. E. et al. *Salmonella* mitigates oxidative stress and thrives in the inflamed gut by evading calprotectin-mediated manganese sequestration. *Cell Host Microbe* **19**, 814–825 (2016).
59. Bolyen, E. et al. Reproducible, interactive, scalable and extensible microbiome data science using QIIME 2. *Nat. Biotechnol.* **37**, 852–857 (2019).

Article

60. McMurdie, P. J. & Holmes, S. phyloseq: an R package for reproducible interactive analysis and graphics of microbiome census data. *PLoS ONE* **8**, e61217 (2013).
61. Wickham, H. et al. Welcome to the Tidyverse. *J. Open Source Softw.* **4**, 1686 (2019).
62. Bolger, A. M., Lohse, M. & Usadel, B. Trimmomatic: a flexible trimmer for Illumina sequence data. *Bioinformatics* **30**, 2114–2120 (2014).
63. Eren, A. M., Vineis, J. H., Morrison, H. G. & Sogin, M. L. A filtering method to generate high quality short reads using illumina paired-end technology. *PLoS ONE* **8**, e66643 (2013).
64. Li, D., Liu, C.-M., Luo, R., Sadakane, K. & Lam, T.-W. MEGAHIT: an ultra-fast single-node solution for large and complex metagenomics assembly via succinct de Bruijn graph. *Bioinformatics* **31**, 1674–1676 (2015).
65. Eren, A. M. et al. Anvio: an advanced analysis and visualization platform for 'omics data. *PeerJ* **3**, e1319 (2015).
66. Hyatt, D. et al. Prodigal: prokaryotic gene recognition and translation initiation site identification. *BMC Bioinformatics* **11**, 119 (2010).
67. Eddy, S. R. Accelerated profile HMM searches. *PLoS Comput. Biol.* **7**, e1002195 (2011).
68. Bateman, A. et al. The Pfam protein families database. *Nucleic Acids Res.* **32**, D138–D141 (2004).
69. Kanehisa, M. & Goto, S. KEGG: Kyoto Encyclopedia of Genes and Genomes. *Nucleic Acids Res.* **28**, 27 (2000).
70. Zhang, H. et al. dbCAN2: a meta server for automated carbohydrate-active enzyme annotation. *Nucleic Acids Res.* **46**, W95–W101 (2018).
71. Langmead, B. & Salzberg, S. L. Fast gapped-read alignment with Bowtie 2. *Nat. Methods* **9**, 357–359 (2012).
72. Li, H. et al. The Sequence Alignment/Map format and SAMtools. *Bioinformatics* **25**, 2078–2079 (2009).
73. Kang, D. D. et al. MetaBAT 2: an adaptive binning algorithm for robust and efficient genome reconstruction from metagenome assemblies. *PeerJ* **7**, e7359 (2019).
74. Zheng, J. et al. dbCAN3: automated carbohydrate-active enzyme and substrate annotation. *Nucleic Acids Res.* **51**, W115–W121 (2023).
75. Zhang, J. et al. Altered synthesis of genes associated with short-chain fatty acids in the gut of patients with atrial fibrillation. *BMC Genomics* **22**, 634 (2021).
76. Aramaki, T. et al. KofamKOALA: KEGG Ortholog assignment based on profile HMM and adaptive score threshold. *Bioinformatics* **36**, 2251–2252 (2020).
77. Morrison, D. J. & Preston, T. Formation of short chain fatty acids by the gut microbiota and their impact on human metabolism. *Gut Microbes* **7**, 189–200 (2016).
78. Devlin, J. R. et al. *Salmonella enterica* serovar Typhimurium chitinases modulate the intestinal glycome and promote small intestinal invasion. *PLoS Pathog.* **18**, e1010167 (2022).
79. Arkin, A. P. et al. KBase: The United States Department of Energy Systems Biology Knowledgebase. *Nat. Biotechnol.* **36**, 566–569 (2018).
80. Heinken, A. et al. Genome-scale metabolic reconstruction of 7,302 human microorganisms for personalized medicine. *Nat. Biotechnol.* **41**, 1320–1331 (2023).
81. Aziz, R. K. et al. The RAST server: Rapid Annotations using Subsystems Technology. *BMC Genomics* **9**, 75 (2008).
82. Henry, C. S. et al. Microbial Community Metabolic Modeling: a community data-driven network reconstruction. *J. Cell. Physiol.* **231**, 2339–2345 (2016).
83. Punta, M. et al. The Pfam protein families database. *Nucleic Acids Res.* **40**, D290–D301 (2012).
84. freiburgermsu & Beilsmith, K. HenryLabResearch/ABX_mouse_gut: Spring 2025 Nature paper (Version v1). Zenodo <https://doi.org/10.5281/zenodo.1497712> (2025).

Acknowledgements The authors thank members of the Chang laboratory for scientific support received. This work was performed with support from US National Institutes of Health (NIH) T32DK007074 (M.S.K.), NIH RC2DK122394 (E.B.C.), NIH T32GM007281 (M.S.K.), InnoHK via the Hong Kong Innovation and Technology Commission, the Host-Microbe and Tissue and Cell Engineering cores of the UChicago DDRC, Center for Interdisciplinary Study of Inflammatory Intestinal Disorders (C-IID)-(NIDDK P30 DK042086), the Gastrointestinal Research Foundation of Chicago, and The Simons Foundation (J.B.). C.S.H., A.F. and K.B. were supported by the KBase project of the U.S. Department of Energy, Office of Science, Office of Biological and Environmental Research (DE-AC02-06CH11357).

Author contributions M.S.K. conceptualized and performed all experiments, data analysis and results interpretation, and wrote the manuscript. A.F., K.B. and C.S.H. developed the metabolic model methodology, analysed the data and interpreted the results. M.C., M.L.S.G., M.K. and C.C. performed WD resilience, intervention and colonization resistance experiments. A.G. performed histopathological analyses for colonization resistance experiments. S.C.N., F.K.C., O.D. and D.R. interpreted results, edited the manuscript and acquired funding. J.B. and E.B.C. mentored the participants, interpreted results, acquired funding and assisted in writing and editing of the manuscript.

Competing interests The authors declare no competing interests.

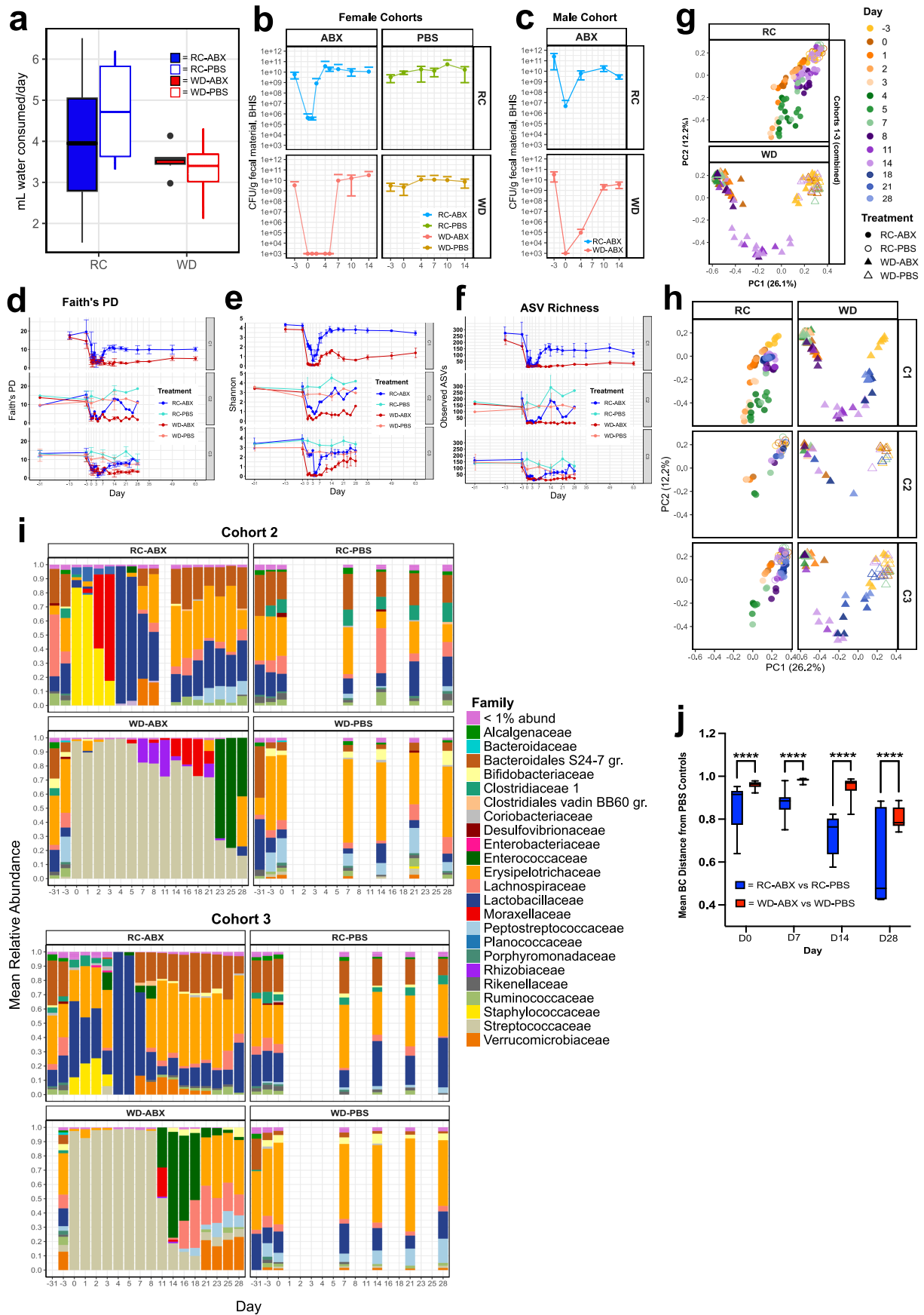
Additional information

Supplementary information The online version contains supplementary material available at <https://doi.org/10.1038/s41586-025-08937-9>.

Correspondence and requests for materials should be addressed to E. B. Chang.

Peer review information *Nature* thanks Jessica Allegretti, Sean Gibbons and the other, anonymous, reviewer(s) for their contribution to the peer review of this work. Peer review reports are available.

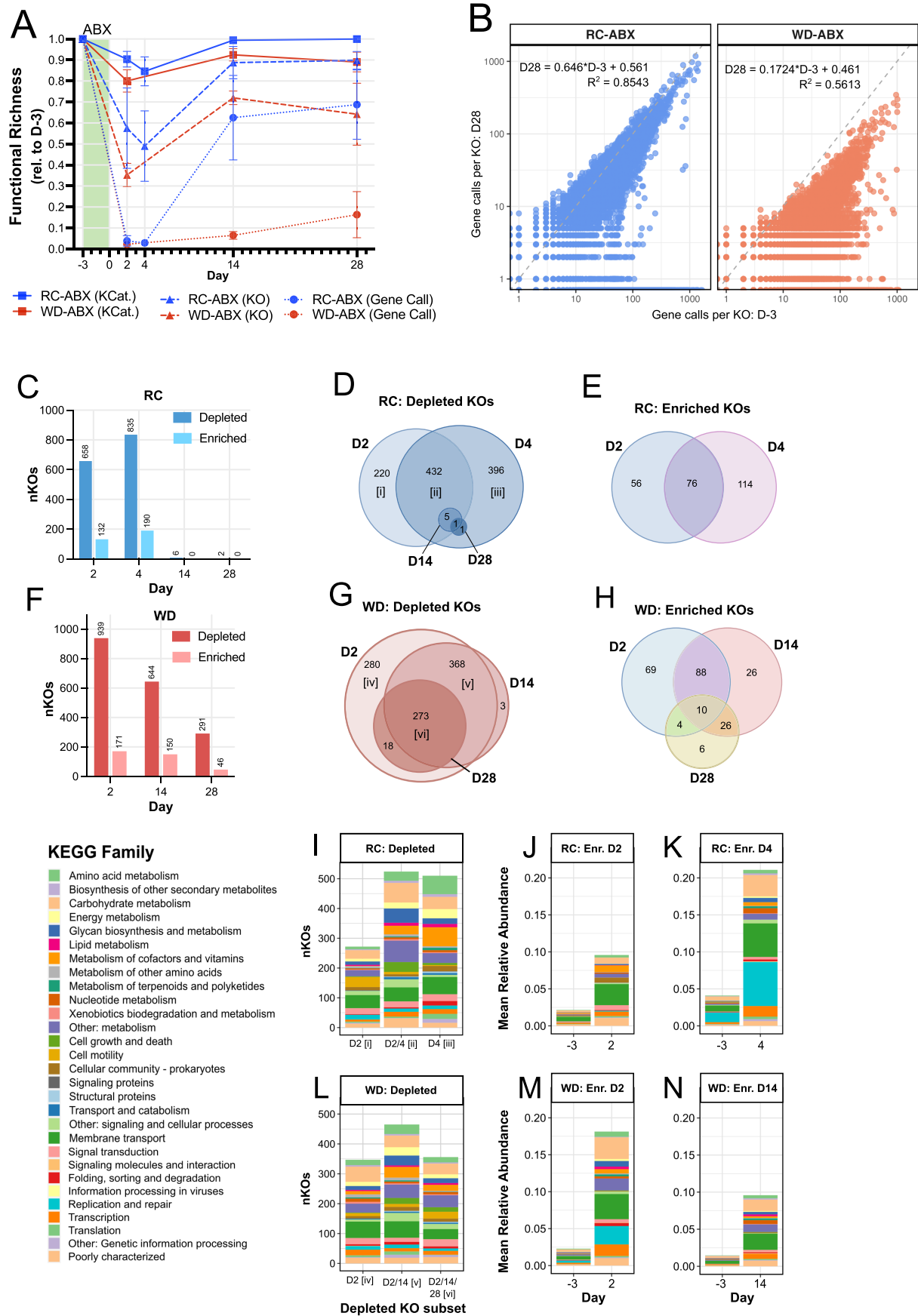
Reprints and permissions information is available at <http://www.nature.com/reprints>.



Extended Data Fig. 1 | See next page for caption.

Article

Extended Data Fig. 1 | Western diet impairs microbiome taxonomic and biomass recovery from antibiotics. (A) Consumption of ABX- or PBS-spiked water per mouse per day did not differ significantly across any treatment groups (RC-ABX $n = 6$ mice; RC-PBS $n = 4$; WD-ABX $n = 6$; WD-PBS $n = 4$; one-way ANOVA). (B-C) Microbial CFUs plated on anaerobic BHIS media from all (B) female ($n = 5-18$ /group/timepoint; exact n values in Table S1A) and (C) male cohorts ($n = 6$ mice/group) through Day 14 of recovery post-ABX. Three of six female cohorts and the male cohort did not undergo 16S analysis as in the rest of Fig. 1; these data are therefore excluded from Fig. 1a and Table S1B, but are analyzed separately in Table S1C. (D-F) Comparison of alpha diversity metrics across cohorts over time; $n = 1-6$ mice/treatment group/cohort/timepoint; exact n values and statistics in Table S2. (D) Faith's phylogenetic diversity; (E) Shannon index; (F) ASV richness. (G-H) PCoA of 16S-based microbiome taxonomic composition at the genus level using Bray-Curtis dissimilarity for samples from all treatment groups; $n = 1-6$ mice/treatment/cohort/timepoint; exact n values in Table S2A. (G) Through D14; Cohort 1 only. (H) Through D28; paneled by experimental cohort.. (I) Mean relative abundances of different microbial families for Cohorts 2 and 3 ($n = 1-3$ mice/treatment/cohort/timepoint, exact n values in Table S2A). (J) Mean Bray-Curtis dissimilarity of antibiotic-treated groups from their respective PBS control groups at each timepoint (** $p < 0.0001$, two-way ANOVA with multiple post-hoc comparisons and FDR correction; Table S2). For boxplots in panels (A) and (I), the middle line is the median, the upper and lower hinges reflect the first and third quartiles, and the whiskers extend to 1.5*IQR. Data beyond the whiskers are plotted as outlying points. In (B – F), data are presented as mean \pm SD.

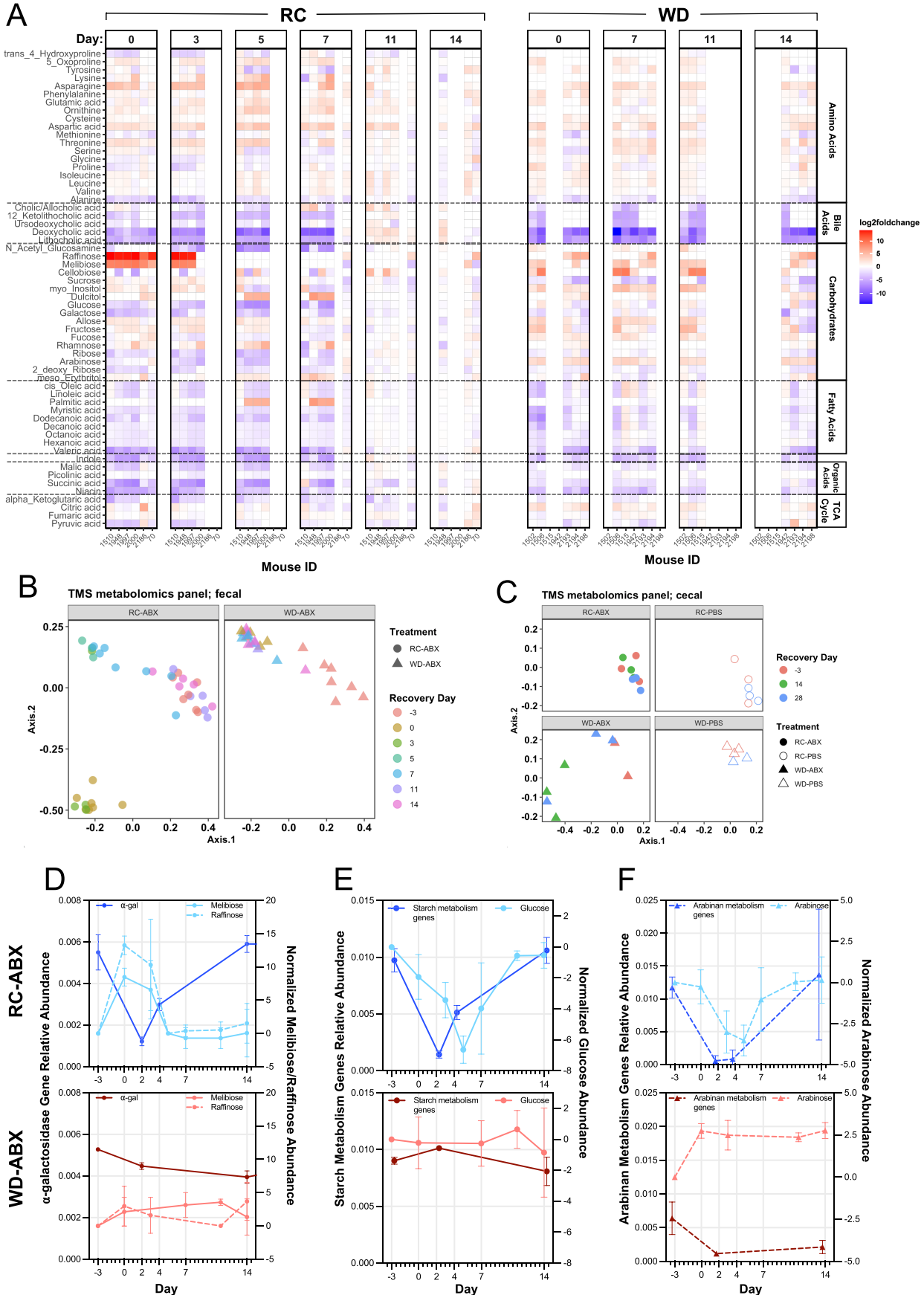


Extended Data Fig. 2 | See next page for caption.

Article

Extended Data Fig. 2 | Microbiome metagenomic recovery dynamics differ across dietary treatments. (A-J) Metagenomic analyses of $n = 2\text{-}8$ mice/treatment/timepoint (RC-ABX D-3: $n = 8$; RC-ABX D2: $n = 2$; RC-ABX D4: $n = 3$; RC-ABX D14: $n = 3$; RC-ABX D28: $n = 3$; WD-ABX D-3: $n = 8$; WD-ABX D2: $n = 3$; WD-ABX D14: $n = 4$; WD-ABX D28: $n = 3$; Table S3). (A) Metagenomic functional richness in fecal samples from mice on RC-ABX (blue) and WD-ABX (red) at the KEGG Category (KCat), KEGG Ortholog (KO), and gene call level as a percentage of functional richness at Day -3 (pre-ABX) (Table S3). Data are presented as mean \pm SD. (B) Initial (Day -3) versus final (Day 28) functional redundancy (genes calls per KO) for mice on RC-ABX (blue) and WD-ABX (red). Each dot represents a unique KO, with X and Y axes representing mean functional

redundancy for that KO averaged across all mice in the respective treatment group/timepoint. (Table S3). For mice on RC-ABX (C-E) or WD-ABX (F-H), counts of significantly differentially abundant KOs (C, F), and Venn diagrams of depleted (D, G) or enriched (E, H) KOs across timepoints. KEGG Family mapping of significantly depleted KOs in mice on (I) RC-ABX or (L) WD-ABX. Roman numerals indicate the subset of KOs depicted in panels (D) and (G). Relative abundances of significantly enriched KOs in mice on RC-ABX at (J) Day 2 and (K) Day 4 relative to Day -3. Relative abundances of significantly enriched KOs in mice on WD-ABX at (M) Day 2 and (N) Day 14 relative to Day -3. See Table S4 for statistics.

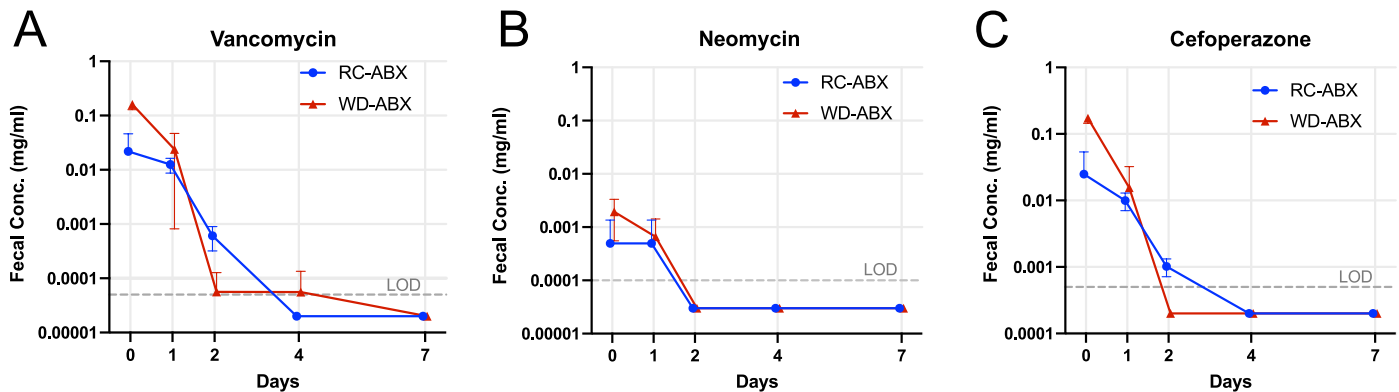


Extended Data Fig. 3 | See next page for caption.

Article

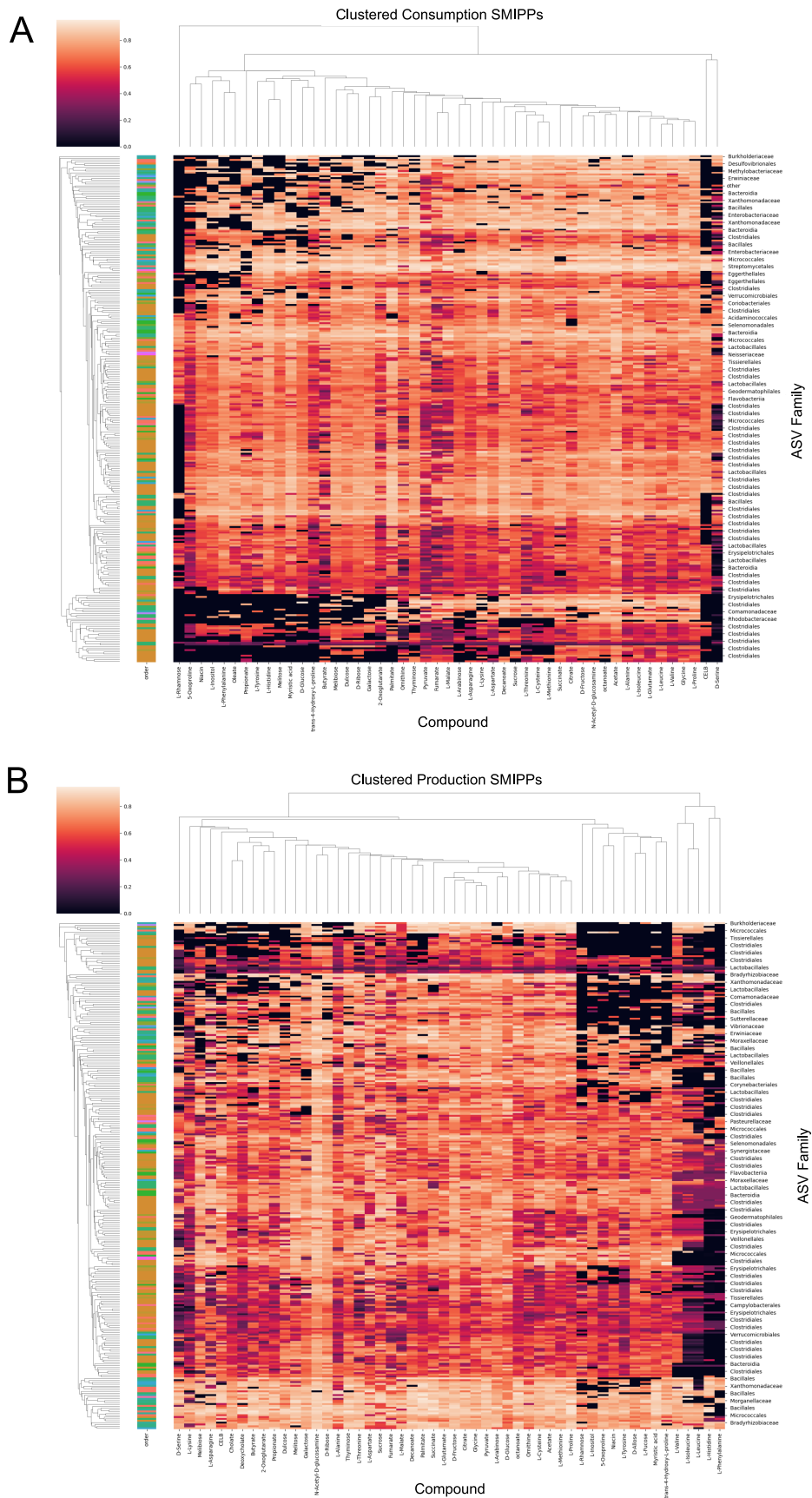
Extended Data Fig. 3 | Metabolomic evaluations show distinct recovery dynamics across diets. (A) Normalized metabolite abundances for mice on RC-ABX at different timepoints are consistent across mice. Each vertical block represents a different day of recovery. Each column within a block represents samples from a different mouse. Abundances are normalized to Day -3 (pre-ABX) for each mouse. (B) PCoA of fecal metabolomics TMS panel data using Bray-Curtis dissimilarity for samples from RC-ABX and WD-ABX through Day 14 of recovery. (C) PCoA of cecal metabolomics TMS panel data using Bray-Curtis dissimilarity for samples from RC-ABX and WD-ABX through Day 28 of recovery.

Cecal samples were used due to availability of material through Day 28. (D – F) Metagenomic gene abundances (left axis, Materials and Methods) and normalized metabolite abundances (right axis) over time for mice on RC (top, blue) and WD (bottom, red). Data are presented as mean \pm SD. $N = 2\text{--}3$ mice/group/timepoint for genes, $n = 3\text{--}6$ mice/group/treatment for metabolites; see Table S6 for exact n values and statistics. (D) α -galactosidase genes, melibiose and raffinose abundance. (E) Starch metabolism genes, glucose abundance. (F) Arabinan metabolism genes, arabinose abundance.

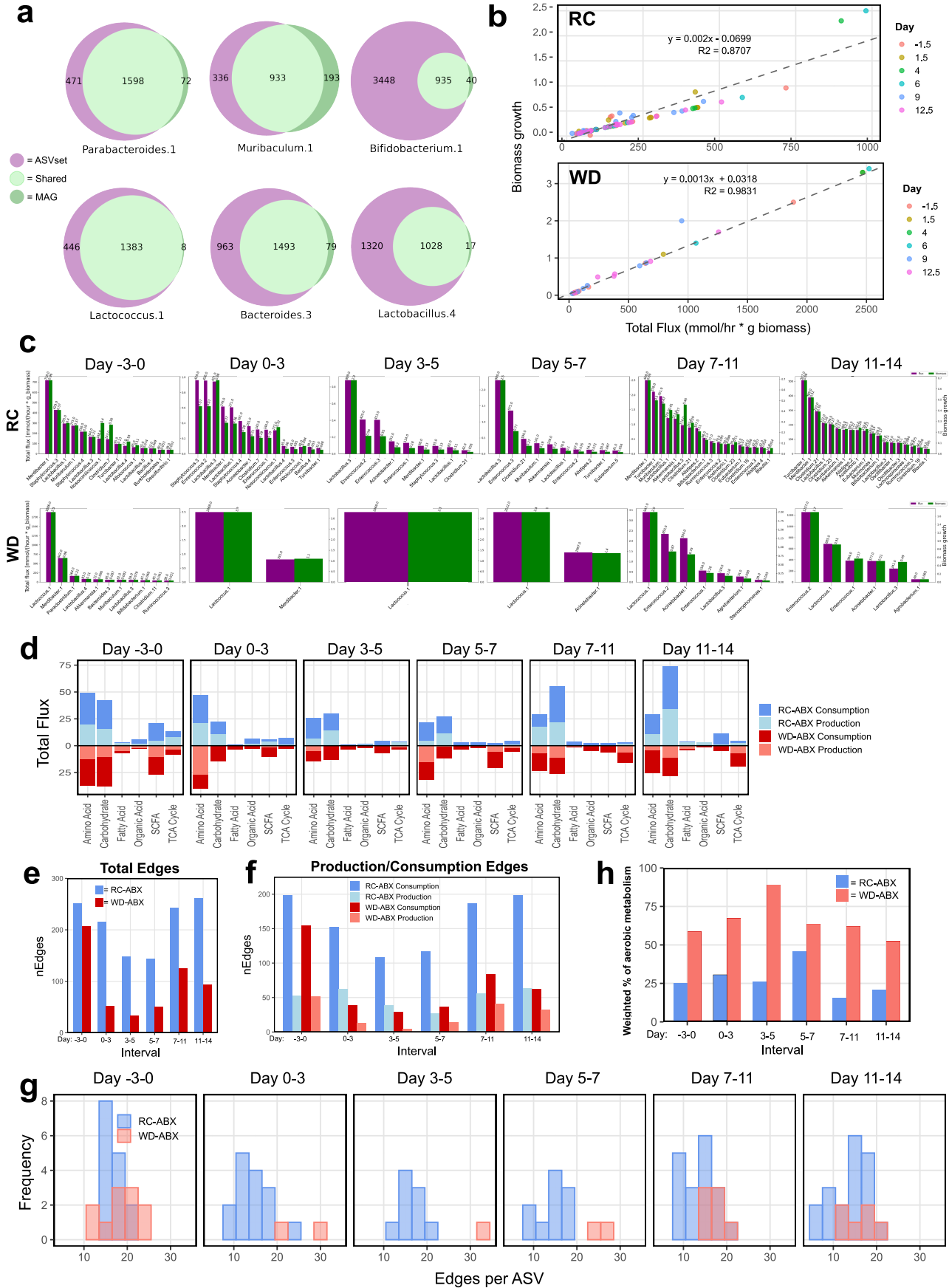


Extended Data Fig. 4 | Residual antibiotic concentrations were not significantly different across RC-ABX and WD-ABX groups. Absolute quantification of fecal (A) vancomycin, (B) neomycin, and (C) cefoperazone from immediately after cessation of antibiotic treatment through Day 7 of

recovery. RC-ABX D0: $n = 3$; RC-ABX D1: $n = 3$, RC-ABX D2: $n = 4$, RC-ABX D4: $n = 4$; RC-ABX D7: $n = 2$. WD-ABX D0: $n = 4$; WD-ABX D1: $n = 4$; WD-ABX D2: $n = 4$; WD-ABX D4: $n = 2$; WD-ABX D7: $n = 2$. Data are presented as mean \pm SD. See Table S7 for statistics.



Extended Data Fig. 5 | Strain-metabolite Interaction Probability Profiles (SMIPPs) reveal metabolic specialization. Heatmaps indicating the probability that a given ASV prGEM (rows) has the capacity to (A) consume or (B) produce the indicated compounds (columns).

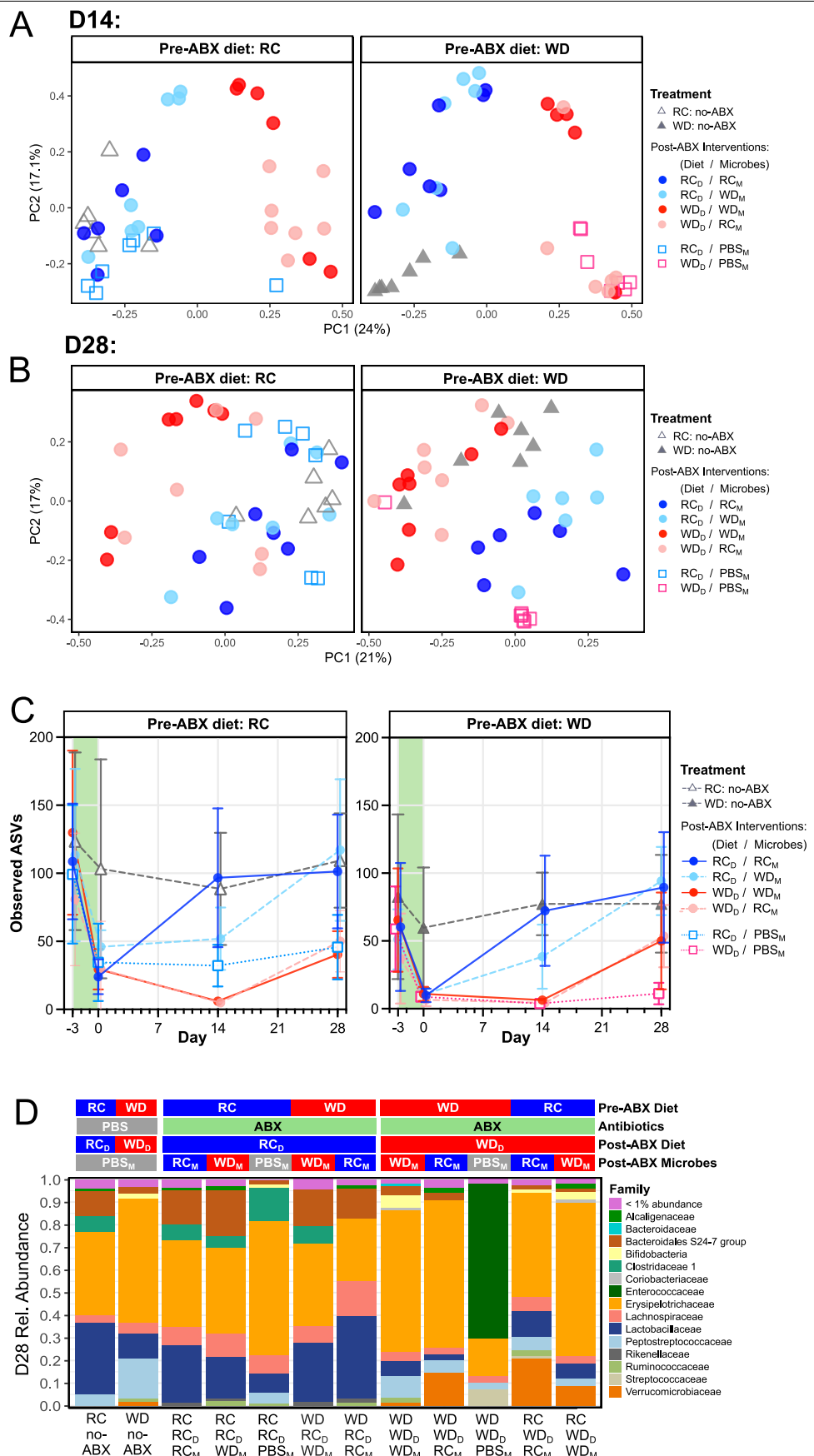


Extended Data Fig. 6 | See next page for caption.

Article

Extended Data Fig. 6 | Community flux simulations vary across dietary treatment groups. (A) Shared and unique functional annotations in ASVset pangenomes and MAGs. (B) Scatterplots of biomass growth vs metabolic flux. Each dot represents a single community member, colored by the time interval. (C) Biomass growth vs metabolic flux for individual community members across diets and timepoints. (D) Total predicted consumption or production flux through each metabolite category in mice on RC (blue, top) or WD (red, bottom) over the indicated recovery interval. As recovery proceeds, mice on RC push more flux through carbohydrate metabolism than mice on WD. (E) Total edges (i.e. metabolic interactions) in the community flux-balance analysis

simulation networks across dietary groups at each time interval, broken down by (F) production or consumption edges. The microbiome of mice on RC has more edges at all timepoints, indicating that they have more/broader metabolite interaction (primarily consumption interactions) than in mice on WD. (G) Histograms depicting the distribution of edges per ASV across diet groups at each time interval. Mice on WD have few taxa that interact with a large number of metabolites, whereas in mice on RC, a broader array of taxa interact with an intermediate number of metabolites. (H) Percent of community metabolism conducted by oxygen-consuming ASVs.

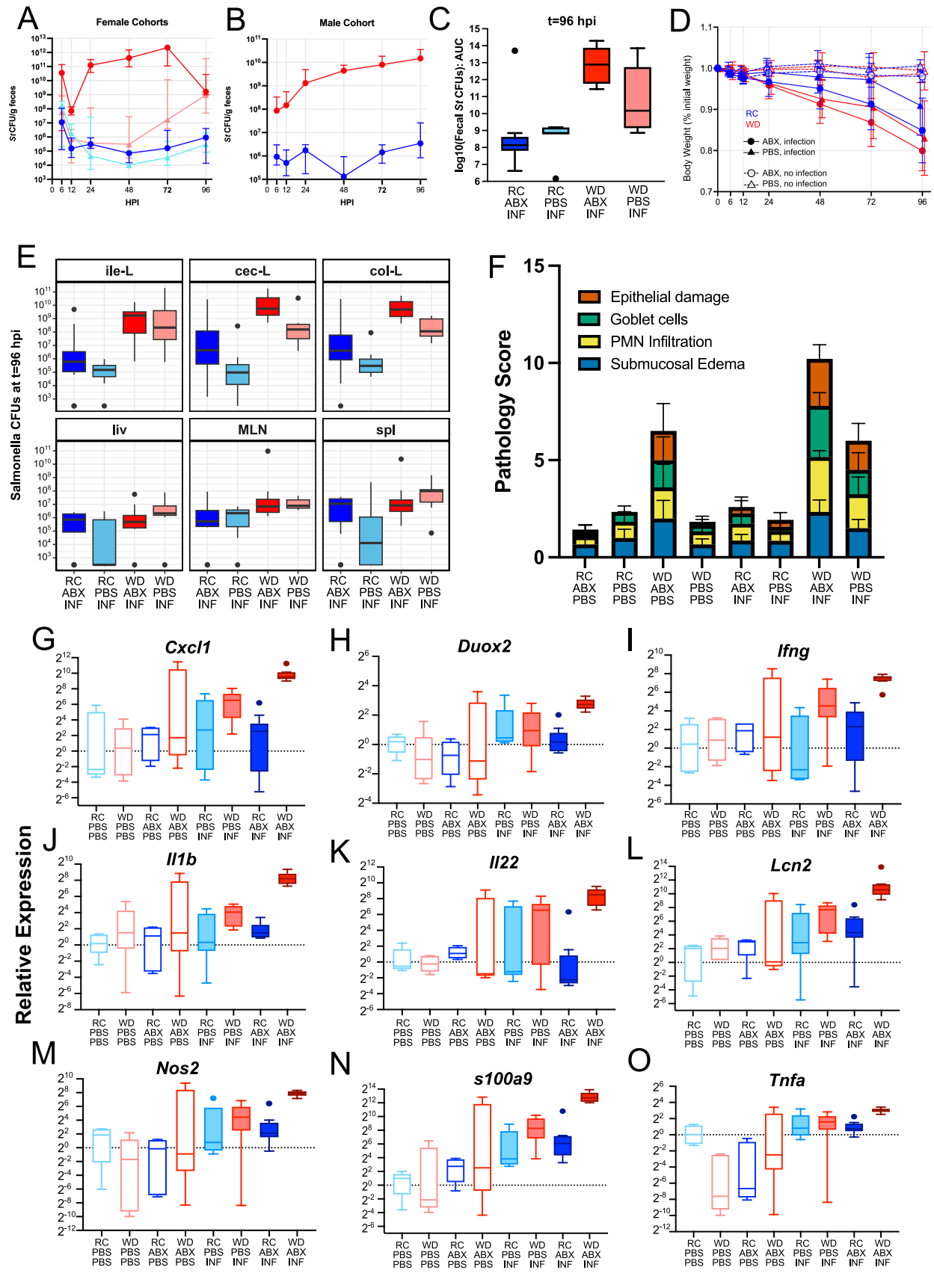


Extended Data Fig. 7 | See next page for caption.

Article

Extended Data Fig. 7 | Dietary intervention and microbial transplant effects through Day 28 of recovery. PCoA plot of 16S-based taxonomic data for mice on all treatment groups at D14 (A) and D28 (B) of recovery. Data is paneled according to pre-ABX diet. (C) ASV richness of all treatment groups through

Day 28 of recovery. Data is paneled according to pre-ABX diet and presented as mean \pm SD. (D) Mean relative abundances of microbial families at Day 28 across treatment groups. Exact n values for (A-D) are presented in table S9A.



Extended Data Fig. 8 | See next page for caption.

Article

Extended Data Fig. 8 | Supplemental information regarding colonization resistance experiments. *N* values for all panels are presented in Table S10A. *St* CFU counts from female (A) and male (B) cohorts through t = 96 hpi. (C) Log10 transformed Infection AUC for all infected treatment groups. (D) Body weight after infection as a percentage of pre-infection body weight for all treatment groups. (E) *St* CFU counts across body tissue sites for all infected treatment groups at t = 96 hpi. (F) Cecal and (G) colonic histopathology scoring of all treatment groups at t = 96 hpi broken down by subscore. (H-P) mRNA expression

of immune genes in cecal mucosal scrapings at t = 96 hpi based on RT-qPCR. Expression is normalized to the housekeeping gene Actb and the RC-PBS-PBS treatment group. See Table S10 for statistics and additional information. In (A), (B), (D), and (F), data are presented as mean ± SD. For boxplots in (C), (E), and (G-O), the middle line is the median, the upper and lower hinges reflect the first and third quartiles, and the whiskers extend to 1.5*IQR. Data beyond the whiskers are plotted as outlying points.

Reporting Summary

Nature Portfolio wishes to improve the reproducibility of the work that we publish. This form provides structure for consistency and transparency in reporting. For further information on Nature Portfolio policies, see our [Editorial Policies](#) and the [Editorial Policy Checklist](#).

Statistics

For all statistical analyses, confirm that the following items are present in the figure legend, table legend, main text, or Methods section.

n/a Confirmed

- The exact sample size (n) for each experimental group/condition, given as a discrete number and unit of measurement
- A statement on whether measurements were taken from distinct samples or whether the same sample was measured repeatedly
- The statistical test(s) used AND whether they are one- or two-sided
Only common tests should be described solely by name; describe more complex techniques in the Methods section.
- A description of all covariates tested
- A description of any assumptions or corrections, such as tests of normality and adjustment for multiple comparisons
- A full description of the statistical parameters including central tendency (e.g. means) or other basic estimates (e.g. regression coefficient) AND variation (e.g. standard deviation) or associated estimates of uncertainty (e.g. confidence intervals)
- For null hypothesis testing, the test statistic (e.g. F , t , r) with confidence intervals, effect sizes, degrees of freedom and P value noted
Give P values as exact values whenever suitable.
- For Bayesian analysis, information on the choice of priors and Markov chain Monte Carlo settings
- For hierarchical and complex designs, identification of the appropriate level for tests and full reporting of outcomes
- Estimates of effect sizes (e.g. Cohen's d , Pearson's r), indicating how they were calculated

Our web collection on [statistics for biologists](#) contains articles on many of the points above.

Software and code

Policy information about [availability of computer code](#)

Data collection

No software was used

Data analysis

The Jupyter Notebooks in which the modeling data was processed and the figures were developed are accessible at https://github.com/HenryLabResearch/ABX_mouse_gut or <https://doi.org/10.5281/zenodo.1497712>.

The following commercial and open-source software was used in our other analyses:

- Graphpad Prism v10.3.1
- R v4.2.1
- QIIME2 v2022.2
- phyloseq v1.40.0
- tidyverse v2.0.0
- Trimmomatic v0.39
- Megahit v1.2.9
- anvi'o v7.1
- Prodigal v2.6.3
- HMMER v3.3
- Bowtie v2.3.5.1
- Samtools v1.11
- MetaBAT 2
- MassHunter Quantitative Analysis vB.10

For manuscripts utilizing custom algorithms or software that are central to the research but not yet described in published literature, software must be made available to editors and reviewers. We strongly encourage code deposition in a community repository (e.g. GitHub). See the Nature Portfolio [guidelines for submitting code & software](#) for further information.

Data

Policy information about [availability of data](#)

All manuscripts must include a [data availability statement](#). This statement should provide the following information, where applicable:

- Accession codes, unique identifiers, or web links for publicly available datasets
- A description of any restrictions on data availability
- For clinical datasets or third party data, please ensure that the statement adheres to our [policy](#)

The data, including all DNA sequencing datasets, that support the findings of this study are available in this article, the Supplemental Information, and BioProject accession PRJNA992061. Metabolomics data are available on the MassIVE database (ID: I000097318) at <ftp://massive.ucsd.edu/v09/MSV000097318/>

Other publicly available datasets used in these analyses include:

KEGG doi.org/10.1093/nar/28.1.27
 EBI's PFAM doi.org/10.1093/nar/gkr1065
 dbCAN CAZyme HMM database doi.org/10.1093/nar/gky418
 dbCAN-sub database doi.org/10.1093/nar/gkad328
 KOFams doi.org/10.1093/bioinformatics/btz859
 AGORA2 doi.org/10.1038/s41587-022-01628-0
 RAST doi.org/10.1186/1471-2164-9-75

Research involving human participants, their data, or biological material

Policy information about studies with [human participants or human data](#). See also policy information about [sex, gender \(identity/presentation\), and sexual orientation](#) and [race, ethnicity and racism](#).

Reporting on sex and gender

N/A

Reporting on race, ethnicity, or other socially relevant groupings

N/A

Population characteristics

N/A

Recruitment

N/A

Ethics oversight

N/A

Note that full information on the approval of the study protocol must also be provided in the manuscript.

Field-specific reporting

Please select the one below that is the best fit for your research. If you are not sure, read the appropriate sections before making your selection.

Life sciences

Behavioural & social sciences

Ecological, evolutionary & environmental sciences

For a reference copy of the document with all sections, see nature.com/documents/nr-reporting-summary-flat.pdf

Life sciences study design

All studies must disclose on these points even when the disclosure is negative.

Sample size	For each experiment, a pilot study was performed and then power analyses were done to determine sample size. Some sample sizes were larger to accommodate destructive sampling in some cohorts at intermediate timepoints before the end of the experiment.
Data exclusions	Sequencing data was excluded if it did not meet quality criteria as described in the methods.
Replication	Each experiment was performed across 3-4 independent cohorts, which generally replicated consistent results. Moreover, similarities of the experimental design across major experiments allowed for comparison of data (i.e. certain treatment groups in the Intervention Experiments were directly comparable to the WD-Resilience experiments, as were the Colonization Resistance experiments before infection at Day 14 of recovery. These further validated the replicability of our results.
Randomization	Mice were randomly assigned to treatment groups for all experiments. Before randomization, all mice across cages were homogenized as much as possible.
Blinding	Investigators were not blinded to group allocation during data collection because the color and texture of the diet itself, as well as the effects of diet on fecal color and consistency, made it impossible to hide which groups were which, and because it was necessary to know which group was which for logistical reasons of actually carrying out the experiments. Because minimal data was analyzed from the time of sample collection (vs after nucleic acid extraction, molecular processing, etc), blinding at the sample collection stage was not critical.

Reporting for specific materials, systems and methods

We require information from authors about some types of materials, experimental systems and methods used in many studies. Here, indicate whether each material, system or method listed is relevant to your study. If you are not sure if a list item applies to your research, read the appropriate section before selecting a response.

Materials & experimental systems		Methods	
n/a	Involved in the study	n/a	Involved in the study
<input checked="" type="checkbox"/>	Antibodies	<input checked="" type="checkbox"/>	ChIP-seq
<input checked="" type="checkbox"/>	Eukaryotic cell lines	<input checked="" type="checkbox"/>	Flow cytometry
<input checked="" type="checkbox"/>	Palaeontology and archaeology	<input checked="" type="checkbox"/>	MRI-based neuroimaging
<input type="checkbox"/>	Animals and other organisms		
<input checked="" type="checkbox"/>	Clinical data		
<input checked="" type="checkbox"/>	Dual use research of concern		
<input checked="" type="checkbox"/>	Plants		

Animals and other research organisms

Policy information about [studies involving animals](#); [ARRIVE guidelines](#) recommended for reporting animal research, and [Sex and Gender in Research](#)

Laboratory animals	C57BL/6 mice of both sexes began experiments at 5 weeks of age. Mice were maintained in standard barrier facilities or gnotobiotic Techniplast IsoCage P Bioexclusion cages with pine shaving bedding. Light cycles are 12/12 light-dark with lights on at 6am and lights off at 6pm. Temperature ranges were maintained between 68-79 F, and humidity was maintained between 30-70%.
Wild animals	No wild animals were used in this study.
Reporting on sex	Studies were primarily performed in female mice to reduce possible variation introduced by sex. One cohort of male mice was analyzed to ensure that results were broadly consistent across sexes (Figure S1, S8).
Field-collected samples	No field-collected samples were used in this study.
Ethics oversight	The University of Chicago Institutional Animal Care and Use Committee oversaw this project. Experiments are described on Animal Care and Use Protocol form 72101.

Note that full information on the approval of the study protocol must also be provided in the manuscript.

Plants

Seed stocks

Report on the source of all seed stocks or other plant material used. If applicable, state the seed stock centre and catalogue number. If plant specimens were collected from the field, describe the collection location, date and sampling procedures.

Novel plant genotypes

Describe the methods by which all novel plant genotypes were produced. This includes those generated by transgenic approaches, gene editing, chemical/radiation-based mutagenesis and hybridization. For transgenic lines, describe the transformation method, the number of independent lines analyzed and the generation upon which experiments were performed. For gene-edited lines, describe the editor used, the endogenous sequence targeted for editing, the targeting guide RNA sequence (if applicable) and how the editor was applied.

Authentication

Describe any authentication procedures for each seed stock used or novel genotype generated. Describe any experiments used to assess the effect of a mutation and, where applicable, how potential secondary effects (e.g. second site T-DNA insertions, mosaicism, off-target gene editing) were examined.